Low- and high-fidelity modeling of sandwich-structured composite response to bird strike, as tools for a digital-twin-assisted damage diagnosis.

E. Giannaros[1], A. Kotzakolios[1], V. Kostopoulos[1,*], G. Sotiriadis[1], R. Vignjevic[2], N. Djordjevic[2], M. Boccaccio[3], M.Meo[3]

[*] ~~corresponding~~ Corresponding author, e-mail: kostopoulos@mech.upatras.gr

Keywords: Bird strike, Composites, Sandwich panel, FEM-SPH, LS-DYNA, Soft body impact, FBG sensors, Digital Twin

Abstract

The constant requirement of aerospace industry to enhance the structural efficiency has driven to the usage of high-performance composite materials, either monolithic or sandwich. However, aerospace composite structures are prone to damage due to high-velocity impact events such as bird strike, hail impact, etc. These impact events can result in extensive damage including structure perforation, which will eventually degrade its post-impact residual strength. Therefore, the early detection of damage in composite structure is imperative to avoid catastrophic failure. This paper develops the computational models which predict the dynamic behaviour of a helicopter composite sandwich structure undergoing a bird strike. The models are aimed to be used as virtual tools for a future digital-twin-assisted fault detection technique. Firstly, a high-fidelity (HF) FE/SPH model was developed in LS-DYNA, and it was validated against the soft body impact experiments. Afterwards, a computationally efficient low-fidelity (LF) model was developed and correlated with the high-fidelity model. It was concluded that the high-fidelity model can sufficiently accurately predict the

[1] Applied Mechanics & Vibrations Laboratory, Department of Mechanical Engineering and Aeronautics, University of Patras, Greece (AML, UPAT).
[2] Mechanical and Aerospace Engineering, Brunel University London, United Kingdom (UBRUN).
[3] Materials and Structures Centre, Department of Mechanical Engineering, University of Bath, United Kingdom (MAST, UBATH)

strain history experimentally recorded by the FBG sensors, and that size of the predicted delamination area at the front face of the sandwich structure agrees very well with the experimentally observed delamination area. It was also shown that the LF model can rapidly predict the global dynamic response of sandwich panel under the impact loading, through the good agreement between the numerical strain histories with the FBG measurements. Consequently, the LF model can be used as a quick numerical guide for the identification of the loading condition, whereas the HF model can be used as virtual damage detector and estimator of damage extension before the scheduled inspection.

1 Introduction

For the last forty years, an escalating usage of composite materials has been observed in aerospace industry both in the monolithic and the sandwich configuration. Initially, they were utilized in non-safety critical components and, recently, in primary components for structural efficiency reasons. Nevertheless, both monolithic and sandwich-structured composites are quite prone to high-velocity impact events. One common and major importance threat in aviation is the bird strike, which can occur during the aircraft take-off, landing or low-altitude flight. Although, according to airworthiness requirements, the aircraft structures exposed to bird strike should be designed to assure capability of continue safe flight and landing, several accidents have been recorded the last decades. On November 10, 2008, Ryanair Flight 4102 from Frankfurt to Rome suffered multiple bird strikes during landing [1]. Both engines and port side landing gear were damaged. In 2009, the US Airways Flight 1549 was landed into Hudson river after the loss of both engines caused by bird strike [2]. In January 2009 in Louisiana, Sikorsky S-76C helicopter crashed, and 8 people died. A 1.1 kg red-tailed hawk fractured the windshield and inserted to the engine fuel control system causing a sudden engine power loss [3]. Also, according to the airworthiness regulations, such as CS -29 for helicopters [4], the compliance to relevant code must be shown by tests, or by analysis based on tests carried out on sufficiently representative structures of similar design. In this field, several studies have been carried out demonstrating and comparing various modeling approaches (Eulerian-Lagrangian approach, Lagrangian or Smoothed Particle Hydrodynamics) for bird strike simulation [5], [6], [7], [8], [9], [10]. Other investigations have focused on the soft-impact response of monolithic composites or sandwich structures [11], [12], [13], [14]. Also, several works have paid special attention to the experimental tests for the explanation of soft-body impact event [15], [16], [17], [18]. Despite the extensive published work in this field, according to the authors' knowledge, the numerical-experimental combined studies on the response of composite structures, particularly the sandwich-structured ones, to soft body impact loading are relatively limited; whereas the detection and estimation of composites damage using digital twin (DT) technology is a brand-new technique that has not been widely used in aerospace industry yet. A few attempts for the integration of digital twin concept to aerospace and space industry are shown below. Tuegel et al. [19] presented a conceptual model using digital twin to predict the aircraft structural life prediction and to assure the structural integrity in flight conditions. Later, in 2012, Glaessgen and Stargel [20] proposed a digital twin paradigm for the prediction of the health and the remaining life of future NASA and U.S air force vehicles. Despite all of that, the digital twin technology is not mature enough for use in the aerospace industry and more development is required.

In the current study, the dynamic response of a curved composite sandwich structure subjected to soft body impact is investigated numerically and experimentally. In particular, the focus is on a segment of front transmission fairing of a helicopter. The objective of the current study is the preparation of two computational models with different fidelity levels and computational costs, aiming at development of a future digital-twin-assisted damage diagnosis. The low- and high-fidelity models are intended to be developed as virtual tools for the early damage detection and the estimation of damage extension during the inspection internals, i.e., before the scheduled maintenance. For the better comprehension of general idea, a schematic of digital-twin-assisted damage diagnosis concept including the function of developed models is shown in Fig. 1. In particular, the FBG sensors data, after impact event, will be collected to a data acquisition system, and then it will be transferred to a data repository system via wireless communication. Afterwards, the evaluation system (onboard or ground processor) will compare the recorded strain history with that of models. The concept is to develop the low-fidelity model (LF) as a quick numerical guide for the identification of impact loading conditions, based on the comparison of the numerically calculated strain history with the real-time data from FBG sensors installed in the physical/operating environment, whereas the high-fidelity (HF) model will be employed as virtual damage detector and estimator.

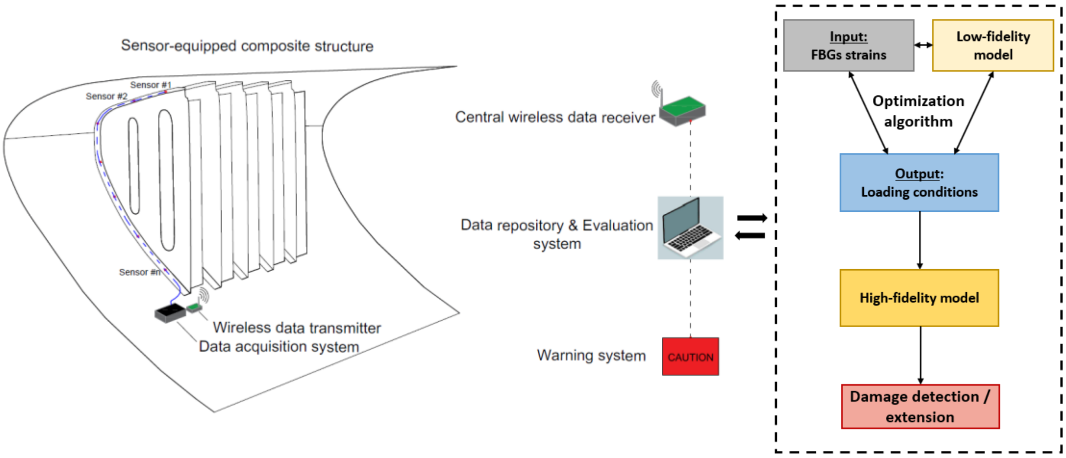

Fig. 1 A schematic of digital-twin-assisted damage diagnosis concept

The digital twin is a cutting-edge technology that has received a lot of attention, which combines several technologies and tools, including Data transmission, collection and processing; Communication-Interaction technology; Modeling-Simulation technology; Sensing-Measurement technology [21]. As presented above, the modeling technology is the main research focus of this study, nevertheless important conclusions can be extracted for the used data recording device (interrogator) and the FBG sensing technology.

2 Panel geometry, materials & manufacturing process

The engine cowling system of a helicopter is geometrically complex and is divided to many curved fairings for design, manufacturing, and maintenance reasons. The current study is focused on the front transmission fairing since the probability of a frontal bird strike is higher than the case of an oblique impact. In the framework of current work, for the sake of simplicity, a small representative segment of front fairing is examined. The design of the cowl segment manufactured by UPAT was inspired by an existing solution used on Agusta Westland AW139. In Fig. 2~~Fig. 2~~, the top and side view of AW139 helicopter including the examined segment of cowling system is given.

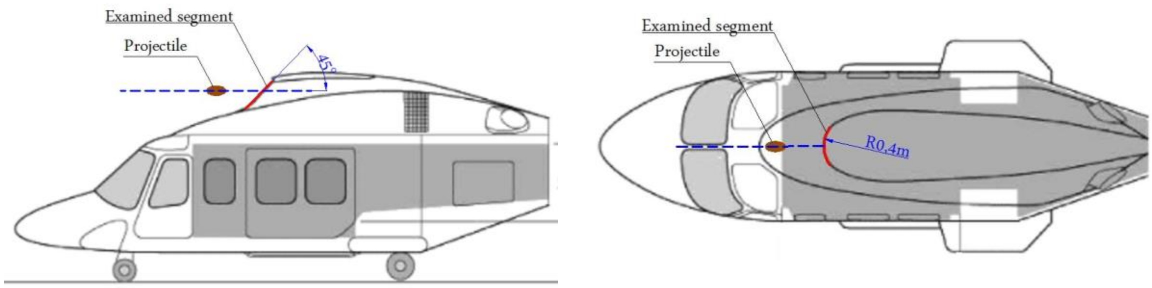

Fig. 2 Top and side view of AW139 helicopter [22] including the examined panel.

The examined sandwich panel is 500 mm in length, 470 mm in width and about 26 mm in thickness. In essence, it is a slightly curved rectangular panel with a radius of 400 mm, whilst it is assumed that it consists of two symmetric quasi-isotropic lay-up ($[(45/0/-45/90)_2]_s$) CFRP faces with 2.88 mm thickness and a 20 mm thick polymer foam layer. The geometry of investigated panel and fiber orientation system is illustrated in Fig. 3~~Fig. 3~~.

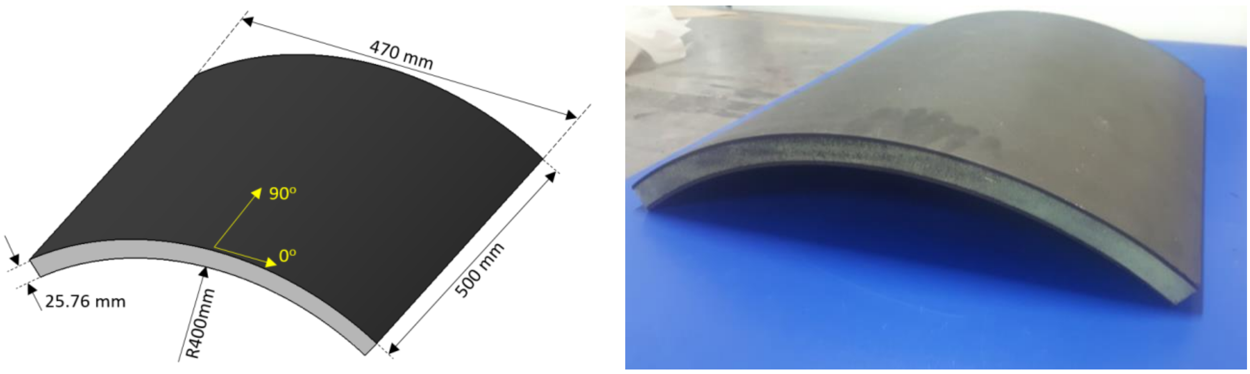

Fig. 3 Composite sandwich panel and fiber orientation system

For the manufacturing of outer faces of sandwich panel, the high-performance aerospace-grade unidirectional Cycom 977-2 carbon fiber reinforced polymer (CFRP) material was used [23]. The matrix constituent is a 177°C curing toughened epoxy resin, whereas the reinforcement consists of intermediate modulus carbon fibers named TohoTenax IMS60. For the characterization of Cycom 977-2 composite, basic quasi-static mechanical and fracture tests have been performed in-house using the UPAT servo-hydraulic machines INSTRON 8872 and 8802. All tests were carried out according the proposed standards for polymer matrix based composite materials [24]. The derived lamina and interlaminar properties of Cycom 977-2 are illustrated in Table 2~~Table 2~~, whereas more information is provided in [24]. Regarding the material of panel core, a closed cell, cross-linked polymer foam with relative high stiffness and strength and low density (AIREX C70.75) is used. According the AIREX manufacturer, it is ideally suitable for a wide variety of lightweight sandwich structures subjected to both static and dynamic loads. The properties of used foam are given in Table 2~~Table 2~~. For the bonding of CFRP skins with foam core, the structural thermal resistant AS 89.1 adhesive supplied by ELANTAS was utilised, which is an aerospace qualified two component epoxy system with good fracture toughness [25]. The shear strength by tension according to ASTM D 1002 (single-lap-joint bonded metals) ranges from 27 MPa to 33 MPa, whereas the tensile strength according to ASTM D 638 is between 50 MPa and 60 MPa [25].

Concerning the manufacturing process of panel, secondary bonding between skins and foam was adopted. Initially, Prepreg/Autoclave process was followed for the preparation of CFRP faces. The manipulation and cutting of prepregs and other consumables, as well as the lamination procedure, were carried-out in a controlled environment of 21°C and 70% relative humidity (R.H). After the final vacuum bagging arrangement, the curved tool was placed in the AML autoclave equipment. In parallel, the supplied AIREX foam sheet was cut to specific dimensions and was thermoformed following the proposed procedure by manufacturer. Then, the CFRP faces and the thermoformed foam sheet were bonded using the epoxy based AS 89.1 adhesive. Afterwards, post-curing process at 60 °C for 2hrs was followed. Finally, C-scan ultrasonic inspection of two panels was executed to identify that the commonly encountered defects, such as ply delamination, porosity, and resin-rich zones, do not exist.

3 Soft body impact tests

Two soft body impact tests were conducted with instrumented composite cowl structures using the gas gun test facility shown in Fig. 4~~Fig. 4~~. The gun consists of gas supply, trigger system, pressure vessel, barrel, sabot stripper and target chamber. The barrel used for this testing is 3m long with a bore 62 mm, which allowed for the maximum diameter of the projectile representing bird to be 50 mm. The impact tests were conducted using artificial gelatine projectiles, manufactured following the M. Lavoie [17], with 10% porosity. The projectiles were cylindrical in shape with 50 mm diameter and 120 mm length. The average mass of projectiles used in the tests was 233g; whilst the material density was 988 $\frac{kg}{m^3}$. The projectiles were launched with, for this purpose designed, sabots. When the gas gun was fired, the projectile-sabot assembly was accelerated towards the end of the barrel, where the sabot was stripped of, so that the only projectile continued flying towards the target plate (Fig. 4~~Fig. 4~~). The projectile/sabot system was aligned with the sabot stripper so that the projectile was released appropriately, with a linear velocity in the impact direction without any angular momentum. Projectile speed just before the impact was determined using the images from high-speed camera shown in Fig. 5~~Fig. 5~~; whilst a camera outside the target chamber was used for recording the impact event. The measured impact velocity of projectile in front of the target in two experiments was equal to 150 m/s. The sequence of the high-speed camera frames of the projectile impact from the initial projectile-target contact until the complete disintegration of projectile is given in section 4.4.3, where it is compared with the numerical results.

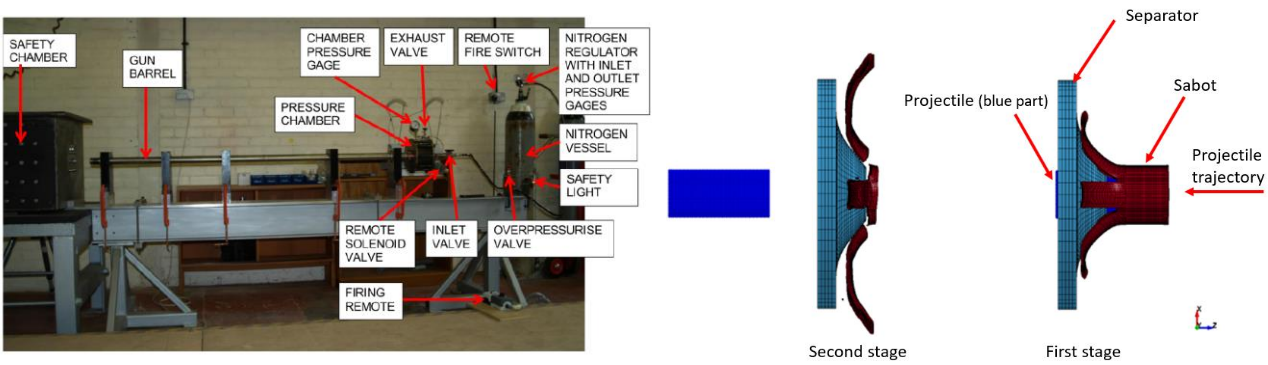

Fig. 4 Gas gun test facility used for the bird strike tests (left), and demonstration of projectile-sabot separation during the test (right)

Both instrumented cowl structures were tested in the same impact conditions, with the target position relative to the impact direction and the boundary condition shown in Fig. 5~~Fig. 5~~. The impact occurred in the middle of the target structure and at angle of 45° relative to the target surface normal.

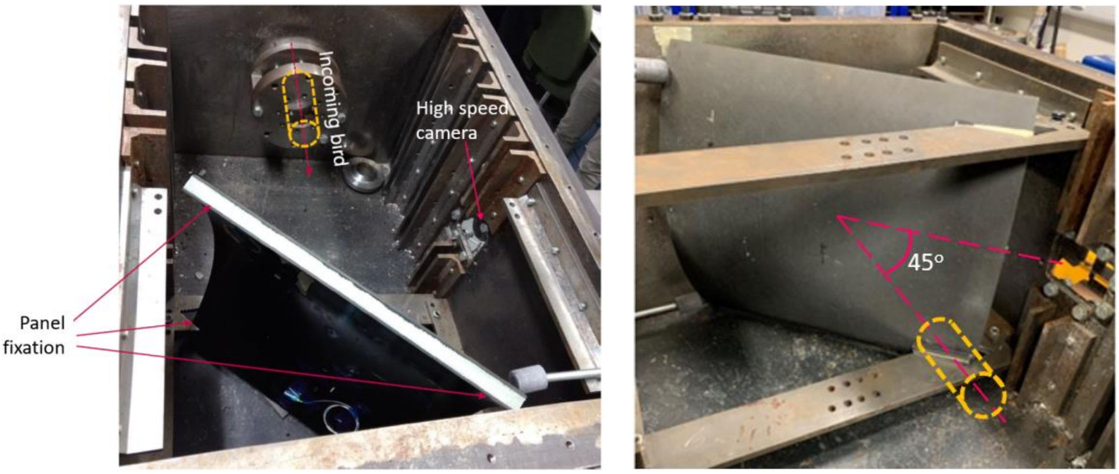

Fig. 5 Panel position and fixture in the target chamber

For the recording of strain histories during the impact event, three Fiber Bragg Grating (FBG) sensors were installed on the back face of the target structure. Each sensor was aligned with specific material direction and was carefully attached to the target face, using a low-viscosity two component epoxy resin. Immediately after the application of the resin, a piece of adhesive tape was placed on the top of the sensor to prevent any resin leakage. The position of sensors is illustrated in Fig. 6~~Fig. 6~~. All sensors were interrogated with the Technobis supergator©, with 19.2 kHz sample rate. The strain component was calculated from the sensor wavelength using Equation 1:

$$\varepsilon = \frac{1}{p_e}\frac{\Delta\lambda}{\lambda_B} \qquad \text{Eq. 1}$$

where $\Delta\lambda$ is load-induced Bragg wavelength shift, λ_B is the Bragg wavelength reflected from the FBG sensor, p_e is the elasto-optic coefficient and ε the applied strain along sensor direction. The interrogator measured the average strain along the sensor length which was 5 mm. The experimental strain measurements used for the model validation are showed in Section 4.4.2.

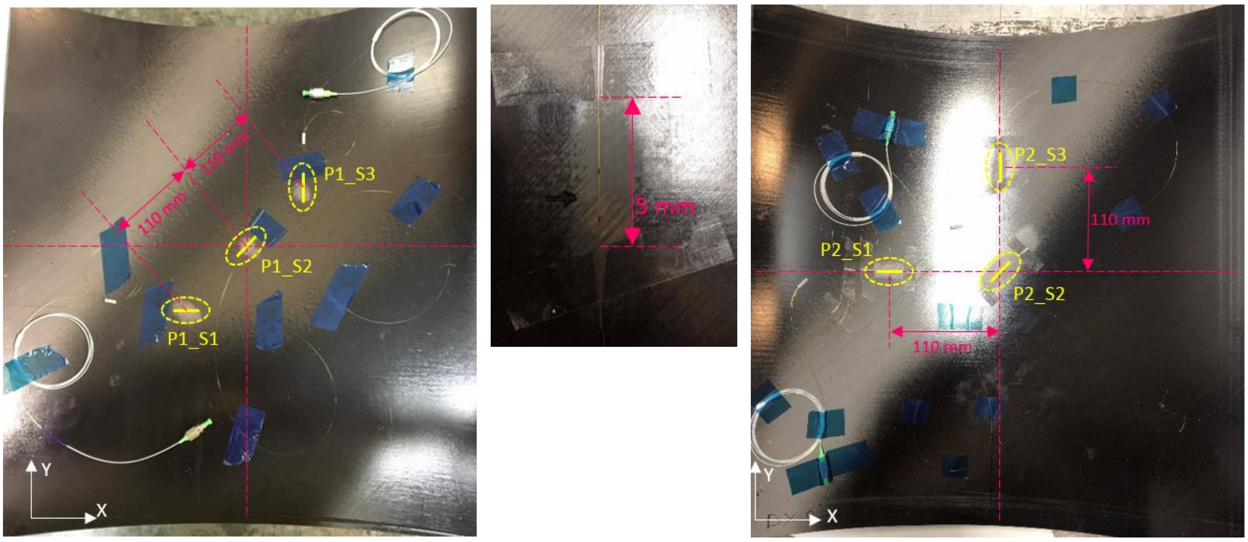

Fig. 6 FBG sensors position (left: panel1, right: panel 2, center: sensor length)

4 Development and validation of high-fidelity (HF) model

In the last decades, several numerical approaches have been used for the simulation of soft body impact. These are the Lagrangian approach, the Arbitrary Lagrangian-Eulerian (ALE) method and the Smoothed Particle Hydrodynamics (SPH). The major drawback of Lagrangian approach is the difficulty to handle the highly distorted elements during the soft body impact, which lead either to prohibitive computational time or to unstable numerical solution. On the other hand, the coupled Lagrangian-Eulerian method can eliminate all difficulties associated with the extreme bird mesh distortion since it allows the finite element to be fixed in space while the material flows though their elements [6]. Nevertheless, the SPH method has been characterized as the most promising formulation since, first, it avoids completely the mesh tangling [9]; additionally, SPH method seems to provide better results in relation to the ALE [5]. For the aforementioned reasons, the current work uses the SPH meshless method to simulate the soft projectile, whereas the target structure is discretized by the traditional Lagrangian finite element formulation. More information about the theory of SPH method is provided to a previous published research of authors [26]; whereas the developed high-fidelity model of sandwich panel is illustrated in Fig. 7~~Fig. 7~~.

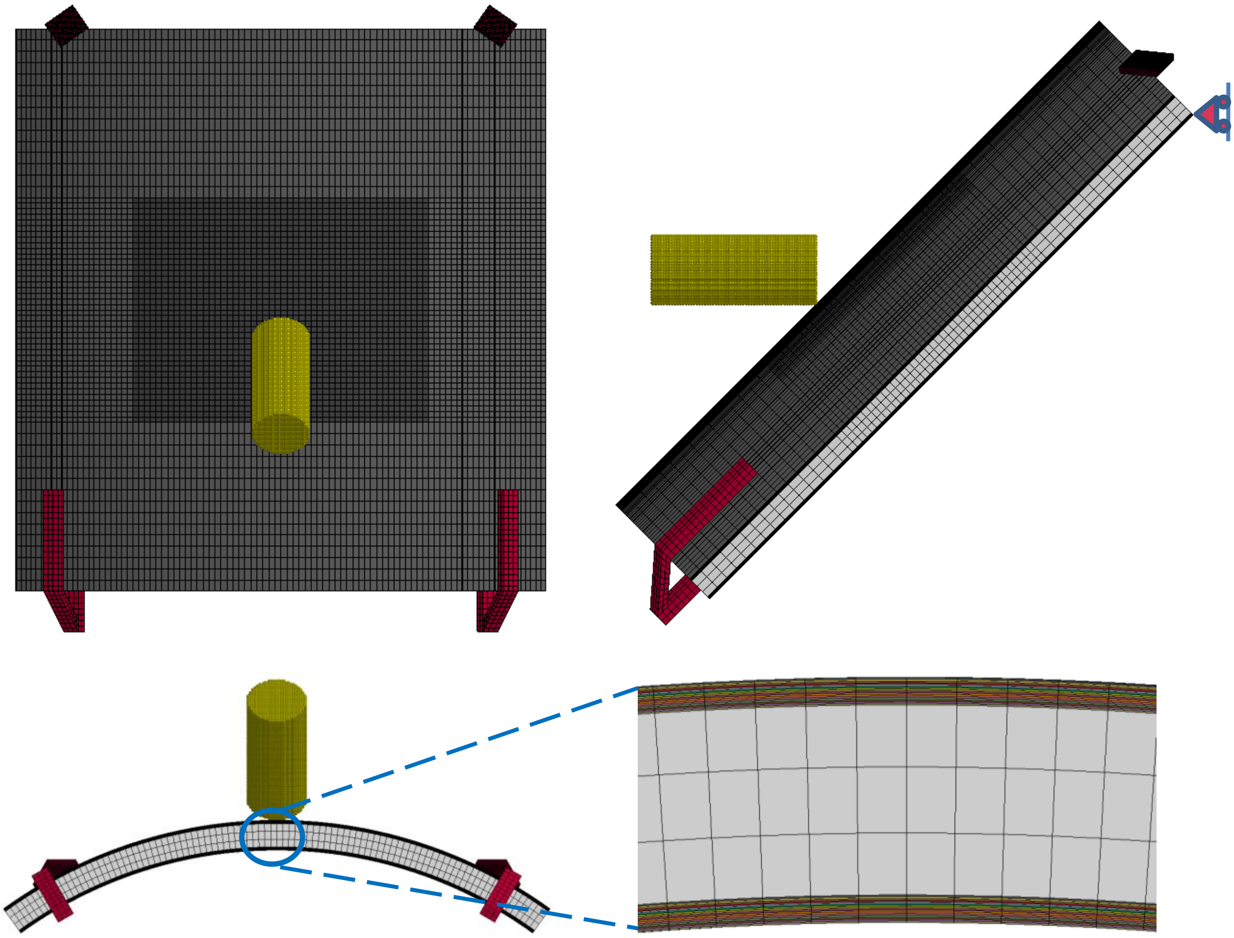

Fig. 7 High-fidelity model

4.1 Modeling of sandwich structure

In general, Finite Element Method is adopted for both CFRP skins and the core of the target structure. In the case of the high-fidelity model, ply-based method (stacked-solid method) with 3D solid elements was adopted for the laminated skins. This technique can predict the separation of laminated plies on the grounds that each lamina is explicitly modelled. Moreover, by the use of solid elements instead of shell elements, no geometric and loading assumptions are required, whereas the boundary conditions are treated more realistically. Also, the solid elements allow the 3D behavior of simulated component to be fully captured. In particular, one fully integrated first-order element formulation (elform 2) per ply was adopted; thus, no hourglass stabilization is needed. However, an elemental error known as shear locking can emerge due to the poor aspect ratio of first-order solid elements in out-of-plane bending conditions. In the case of foam part, for time efficiency reasons, reduced integration solid element with hourglass stabilization is used. The verification of the used element formulations is presented in Section 4.3.1. For delamination initiation and propagation modelling, cohesive zone methodology (CZM) was applied at each interface. The main advantage of CZM method against to the virtual crack-closure technique is that the location of delamination onset does not need to be predefined [27], [28]. Specifically, a fracture-based contact algorithm is utilized at each lamina interface since it eliminates the drawbacks of cohesive elements, including i.e. the reduced time step of solution due to Courant-Friedrichs-Lewy condition, the demand for additional contact between laminas to eliminate plies overlapping after failure of cohesive elements, and the adjustment of their compressive stiffness [29], [30]. Regarding the meshing, relatively higher density mesh is generated near the impact zone (elements size: 5 mm x 5 mm x single-ply-thickness), whereas coarser mesh is adopted away from the impact point for the reduction of computational time (elements size: 10 mm x 5 mm x single-ply-thickness). In the case of foam core modeling, the three solid elements (elform 1: one integration point elements) in through the thickness direction are considered adequate for capturing the bending and shear stiffness of panel (Fig. 7~~Fig. 7~~). The verification checks are illustrated in section 4.3.1.

Regarding the constitutive laws and failure criteria, the Table 1~~Table 1~~ provides the used LS-DYNA material model for each material.

Material	**Type of failure**	**Type of material model**
CFRP	Intralaminar behavior	MAT_ENHANCED COMPOSITE DAMAGE (MAT_54)
	Interlaminar behavior	Fracture-based contact-option 9. It is based on MAT_COHESIVE_GENERAL (MAT_186)
Polyvinylchloride (PVC) foam	Compression & shear failure	MAT_HONEYCOMB (MAT_026)

Table 1. Used material models for composite sandwich panel

According to LS-DYNA documentation [29], the material models of interest capable of representing orthotropic constitutive law with the failure criteria and taking into account damage effects, are the following: 1) Enhanced Composite Damage (MAT_54), 2) Laminated Composite Fabric (MAT_58), 3) Rate-Sensitive Composite Fabric (MAT_158), 4) Composite MSC (MAT_161) for which special license required, 5) Orthotropic Simplified Damage (MAT_221) and 6) Laminated Fracture Daimler (MAT_261-262). However, only MAT_54, MAT_161, MAT_221, and MAT_261-262 are compatible with 3D solid elements. The current study focused on MAT_54 since it provides more simplified damage model than the others while it can capture the most significant failure modes: a) Tensile fiber mode, b) Compressive fiber mode, c) Tensile and d) Compressive matrix mode. The MAT_54 includes two criteria for tensile fiber mode; the first one is the original Hashin criterion which is activated using the β factor equal to 1, whereas the second one constitutes a modification of Hashin criterion. In current study, the modified criterion is applied since the inclusion of the shear stress term in original Hashin tensile fiber criterion underpredicts the peak failure load of cross-ply and quasi-isotropic laminate to tension loading according to literature [31], [32]. The failure criterion equations are the following:

- tensile fiber mode: $\left(\frac{sigma_{aa}}{X_T}\right)^2 = 1$ Eq. 2
- compressive fiber mode: $\left(\frac{sigma_{aa}}{X_C}\right)^2 = 1$ Eq. 3
- tensile matrix mode: $\left(\frac{sigma_{bb}}{Y_T}\right)^2 + \left(\frac{sigma_{ab}}{S_{ab}}\right)^2 = 1$ Eq. 4
- compressive matrix : $\left(\frac{sigma_{bb}}{2\times S_{ab}}\right)^2 + \left[\left(\frac{Y_C}{2\times S_{ab}}\right)^2 - 1\right]\frac{sigma_{bb}}{Y_C} + \left(\frac{sigma_{ab}}{S_{ab}}\right)^2 = 1$ Eq. 5

where $sigma_{aa}$=normal stress in longitudinal direction (fiber), $sigma_{bb}$=normal stress in transverse direction (matrix), $sigma_{ab}$=in-plane shear stress, *b* is the parameter for failure criterion determination, X_T longitudinal tensile strength (fiber), X_c longitudinal compression strength (fiber), Y_c transverse compressive strength (matrix), Y_T transverse tensile strength (matrix), S_{ab} shear strength in-plane. The moduli and strength values for Cycom 977-2 are provided in Table 2~~Table 2~~; whereas, the applicability of the used orthotropic material model as well as the necessary model's parameters for simulating the Cycom 977-2 behavior to impact loading have been thoroughly examined in a previous research of the authors [24]. The cohesive material model in the present investigation was also based on the previous study of authors [24]; in which it has been proved that the MAT_186 using bilinear traction-separation law and 2D power law as fracture criterion can accurately represent the inter-layer behavior of Cycom 977-2 to mode I and mode II. The optimal set of cohesive model's parameters has been obtained using a multi-stage calibration routine. The traction-separation law in MAT_186 is defined by the following parameters: a) interlaminar fracture toughness energy to mode I (G_{IC}), b) normal peak traction (T), c) interlaminar fracture toughness energy to mode II (G_{IIC}), d) shear peak traction (S), e) the normalized separation at peak traction (λ_o), f) exponent of power law mixed-mode criterion (*xmu*); all of which had been considered unknown parameters of calibration problem. The values of these parameters for Cycom 977-2 are shown in Table 2~~Table 2~~, and they are applied indistinguishably to the developed HF model. No strain rate effects of the CFRP were considered in the framework of current work.

Cycom 977-2 CFRP	Value	Unit	**AIREX C70.75 foam**	Value	Unit
Elastic moduli, E_a, for tension	191	GPa	Average density	80	Kg/m^3
Elastic moduli, E_b, for tension	8.85	GPa	Compressive modulus	80	MPa
Elastic moduli, E_a, for compression	121	GPa	Shear modulus	50	MPa
Elastic moduli, E_b, for compression	8.73	GPa	Tensile modulus	50	MPa
Poisson's ratio ν_{ab}	0.258	-	Compressive strength	1.10	MPa
Poisson's ratio ν_{bc}	0.33	-	Shear strength	1.0	MPa
In-plane shear modulus, Gab	4.41	GPa	Shear elongation at break	10	%
Out of plane shear modulus, Gac	4.22	GPa	Tensile strength	1.6	MPa
Tensile strength in fiber axis (X_T)	3325	MPa	**AS 89.1 epoxy adhesive**		
Compressive strength in fiber axis (X_C)	910	MPa	Shear strength (SFLS)	27-33	MPa
Tensile strength in matrix axis (Y_T)	68	MPa	Tensile strength (NFLS)	50-60	MPa
Compressive strength in matrix axis (Y_C)	170	MPa			
Shear strength in ab plane (S_{ab})	81.0	MPa			
Nonlinear shear stress parameter (ALPH)	0.01	-			
Fracture toughness energy to mode I	347.1	J/m^2			
Fracture toughness energy to mode II	571.0	J/m^2			
Peak traction in normal direction (T)	2.0	MPa			
Peak traction in tangential direction (S)	16.94	MPa			
Normalized separation at peak traction	0.5	-			
Exponent of power law mixed-mode	2.0	-			

Table 2. Mechanical properties of used materials and models' parameters [23], [33], [25]

Regarding the material model of polymer foam, LS-DYNA includes more than 15 material models for the simulation of a foam material response [29]. In the framework of current work, special attention was given to MAT_HONEYCOMB (MAT_026) since it can describe the elastoplastic behavior of foam material separately for all normal and shear stresses, and these are fully uncoupled.

Hence, two bilinear stress-strain curves were defined for the case of PVC foam using the datasheet properties of used foam (Table 2~~Table 2~~): one curve for three normal stresses and one for all shearing stresses considering it isotropic. This approach provides the advantage to determine the compression and shear failure strain explicitly. According to R. Wang [34], the AIREX C70.75 foam present similar modulus to both quasi-static and high strain rate compression loading (4400 /s), whereas the dynamic peak stress is slightly higher than the peak stress observed for quasi-static strain rate tests. Therefore, the strain rate dependency on foam properties was considered negligible. Also, they presented that AIREX C70.75 has similar compressive response in three directions, therefore the above consideration about the isotropy behavior is true. The verification checks for material model input data are provided in section 4.3.2.

Finally, surface to surface tiebreak contact algorithm is implemented between the interface of CFRP skin and foam for the skin-core debonding modeling. In particular, the interface nodes are initially tied until the stress-based failure criterion is met. The tiebreak failure criterion has normal and shear component according to the following equation:

$$\left(\frac{|\sigma_n|}{NFLS}\right)^2 + \left(\frac{|\sigma_s|}{SFLS}\right)^2 \geq 1 \qquad \text{Eq. 6}$$

where *NFLS* is the normal strength and *SFLS* is the shear strength. The strength values are taken equal to the minimum adhesive properties given in Table 2~~Table 2~~.

4.2 Modeling of gelatine projectile

As previously described, the gelatine bird's substitute was modelled using SPH particles. In particular, two SPH gelatine models with different particles size are created and evaluated. The first model consists of 1920 particles with initial particle distance (PD) equal to 5 mm, each having a lumped mass 0.1213 g; and the second one contains 29340 particles with 2 mm PD, each having a lumped mass of 0.00794 g (Fig. 8~~Fig. 8~~). The length and diameter of cylindrical projectile are kept equal to the actual ones.

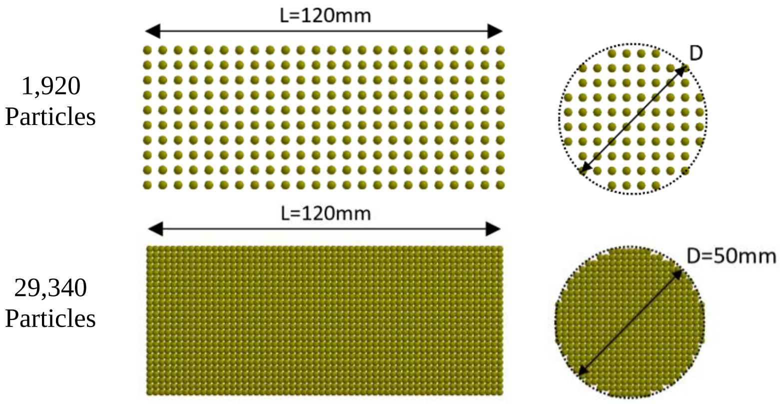

Fig. 8 SPH model of gelatine projectile

Regarding the SPH parameters, according to [26], the most influential parameters are: a) the mathematical parameter (CLSH in LS-DYNA), which is a scale factor of initial particle distance, is used for the calculation of initial smoothing length and influences the support domain of smoothing function; and b) the FORM parameter which defines the particle approximation theory [35]. It has been shown that a high CLSH value (1.5÷2.0) can eliminate the numerical failure due to tensile instabilities, whereas the renormalized approximation theory (FORM=1) improves the accuracy of derivative estimation of a field function [26], [36], [37]. In the framework of current work, the influence of these parameters was examined below using a virtual compression test; and it is concluded that the above consideration is true and useful for the validity of model. Regarding the constitutive equations for birds, much effort and significant progress have been made to develop representative material models according to the review paper [38]. It has been found that the real birds behave as fluids during the impact at velocities larger than 75 m/s, and a gelatine substitute with 10 percent porosity is recommended [15], [39]. In our case, the percent porosity of gelatine substitute is about 1% and the density is equal to $988\frac{kg}{m^3}$, therefore it can be modelled as water. Investigating the relative literature, several modeling approaches have been applied during the last decades [9], [6], [38], [40], [8]: a) the bird can be assumed to be inviscid fluid (such water) using an equation of state (linear, polynomial, tabulated, Gruneisen or Murnaghan EOS), b) modeling of the soft body as elastoplastic material [13], c) using viscous fluid models combined with an EOS. This study was focused on the first modeling approach using a hydrodynamic material model (*MAT_null of LS-DYNA) without viscosity and linear EOS, where the pressure is defined as:

$$P = K \times \left(\frac{\rho}{\rho_o} - 1\right) \qquad \text{Eq. 7}$$

where P is the pressure, K is the bulk modulus (2,200 MPa for water [38]), ρ is the density of material and ρ_o is the reference density at which the material has no pressure ($988\frac{kg}{m^3}$ for water). The null material model relates the stress and strain of the bird by the following:

$$\sigma_{ij} = -P\delta_{ij} + 2\mu\dot{\varepsilon}_{ij} \qquad \text{Eq. 8}$$

where P is the fluid pressure, δ_{ij} is the volumetric stress tensor and $2\mu\dot{\varepsilon}_{ij}$ the deviatoric part which is computed for nonzero dynamic viscosity μ. In this study, the second part of equation is neglected as the water viscosity is considered relatively low. The verification of used modeling approach is demonstrated in the section 4.3.4.

4.3 Verification of numerical uncertainties

4.3.1 Panel stiffness verification

This section presents the verification check of the sandwich panel stiffness. It targets to investigate the influence of used mesh density and element formulation on the maximum deflection of sandwich structure. A 300 N uniformly distributed load along the beam width was applied in the middle of the beam, subjecting it to 3-point bending. The investigated geometry constitutes a small representative sample of sandwich panel model with the same length and thickness (Fig. 9~~Fig. 9~~).

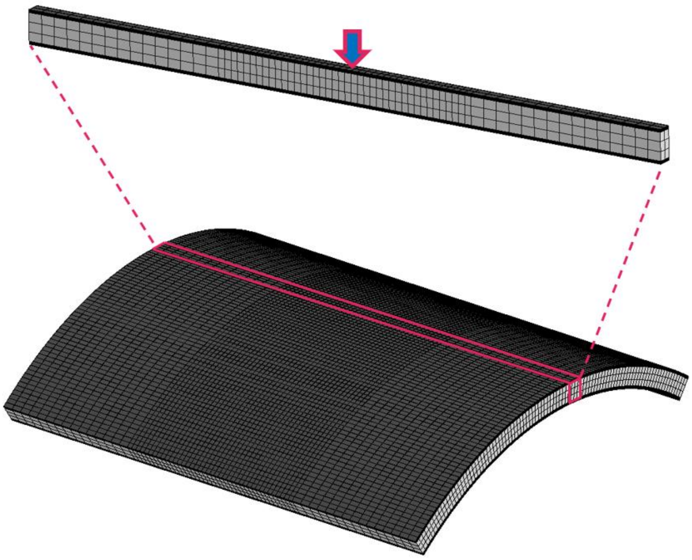

Fig. 9 Representative sample examined for panel stiffness verification

For the calculation of numerical deflection, the implicit nonlinear static solver of LS-DYNA was used; whilst the maximum theoretical deflection for the simply supported beam, δ_{tot}, to 3-point bending can be found by the following equations. According to sandwich beam theory, if the core is weak, $E_c << E_f$, then the transverse shear stress can be approximated as constant in the core [41]. The above assumption is valid since the maximum divergence between numerical results and theoretical ones is 3% approximately (Table 3~~Table 3~~).

$$\delta_{tot} = \delta_b + \delta_s \qquad \text{Eq. 9}$$

$$\delta_b = \frac{P * l^3}{48 * (EI)_{eq}} \qquad \text{Eq. 10}$$

$$(EI)_{eq} = E_f \frac{bt_f^3}{6} + E_f \frac{bt_f d^2}{2} + E_c \frac{bt_c^3}{12} \qquad \text{Eq. 11}$$

$$\delta_s = \frac{P * l}{4 * (AG)_{eq}} \qquad \text{Eq. 12}$$

$$(AG)_{eq} = \frac{b * d^2 * G_C}{t_c} \qquad \text{Eq. 13}$$

where δ_s is the deflection due to shear, δ_b the deflection due to bending, *P* the applied load, *l* the length of beam, *b* the beam width, E_f is the Young's modulus of faces, E_c is the Young's modulus of core,

G_c is the shear modulus of core, t_f the thickness of faces, t_c is the thickness of core and d is the total thickness of beam.

No	Calculation Method	Elem. formulation of skin (thick shell or solid)	Element size to mm (skin)	No of elem. / skin thickness	Elem. formulation of foam (solid)	No of elem. / core thickness	Deflection (mm)
-	Theoretical	-	-	-	-	-	6.75
1	FEM	Thick shell 5	Min: 5 x 5 x t_f Max:10 x 5 x t_f	1	elform 2	3	6.75
2	FEM					6	6.78
3	FEM	Thick shell 3				3	6.82
4	FEM	Thick shell 5					6.73
5	FEM			2			6.71
6	FEM			1	Reduced integration linear solid (elform 1)		6.75
7	FEM	Fully integrated linear solid (elform 2)	Min: 5 x 5 x t_{ply} Max:10 x 5 x t_{ply}	16			6.89
8	FEM			16	elform 2		6.89

Table 3. Comparison of numerical and theoretical deflection

Observing the summary results in Table 3~~Table 3~~, firstly, it is inferred that no shear locking exists using fully integrated linear solid elements since the simulation provides a 2% overprediction of theoretical value (No 8). Secondly, the deflection of one thick shell formulation 5 through the skin thickness is line with the theory (No 1, 6); therefore, it is a promising element formulation for the case of low-fidelity model as it significantly reduces the computational time. Based on this simulation programme, the mesh influence on maximum deflection is negligible.

4.3.2 Verification of foam material model (MAT_26)

In this paragraph, the numerical tests for the verification of foam material model were illustrated. A single reduced integration solid element was tested to compressive and shear loading up to the ultimate failure. The output stress-strain responses in both cases were recorded; and the initial stiffness, yield strength and ultimate strain were compared with the input values derived by material datasheet (Table 2~~Table 2~~).

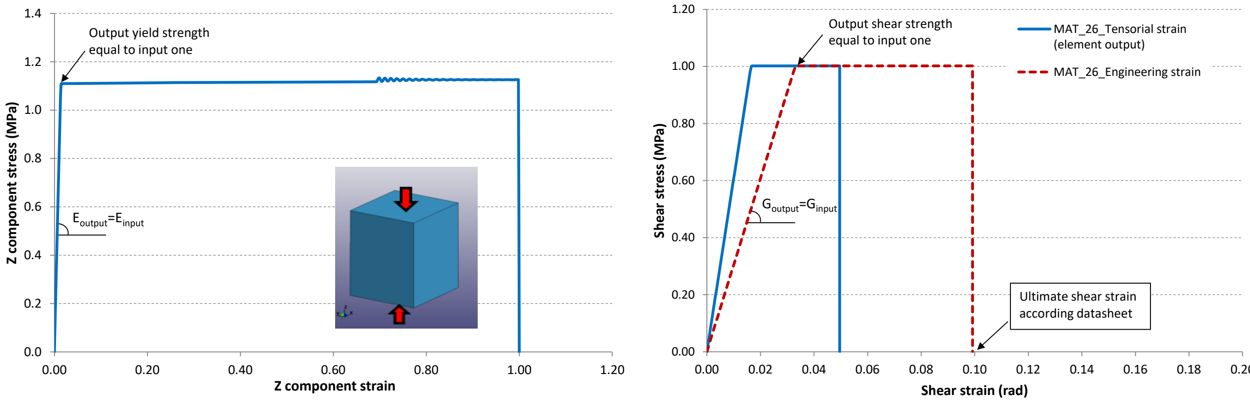

Fig. 10 Stress-strain response of a single element subjected to compressive and shear loading.

Comparing the Fig. 10~~Fig. 10~~ results with the input data (Table 2~~Table 2~~), it is concluded that the material model combined with reduced integration element formulation is capable of capturing the elastoplastic behavior of foam material. In particular, excellent agreement on initial stiffness, yield point and ultimate strain exists between the input and output data. This step was necessary to demonstrate that the user-defined input curves (stress-strain) has been set appropriately.

4.3.3 Verification of SPH parameters

This section is devoted to the identification of the values of the most influential SPH parameters presented above (CLSH and FORM). In the framework of current work, the influence of these parameters was examined to uniaxial compression loading since it is the main loading condition during the impact event. Essentially, a cylindrical elastic body modelled from uniformly distributed SPH particles was chosen to examine. The dimensions, the number of particles and the distance between them were assumed equal to the first gelatine model of Fig. 8~~Fig. 8~~. The aim, here, is to determine the values of SPH parameters which eliminate the numerical failures while an elastic constitutive law with no failure criteria has been adopted. Fig. 11~~Fig. 11~~ shows the influence of each parameter on the compressive stiffness of model. It is observed that the renormalized formulation with Eulerian kernel (FORM 1) is close to both the renormalized Lagrangian formulation (FORM 8) and the theoretical curve. For small values of CLSH parameter, numerical failure (red dashed line) is observed, whereas, considering a value of 1.5 or higher one, the numerical results improvement is visible. For the rest of this paper, the renormalized no fluid Eulerian formulation (FORM 1) with CLSH equal to 1.5 is adopted.

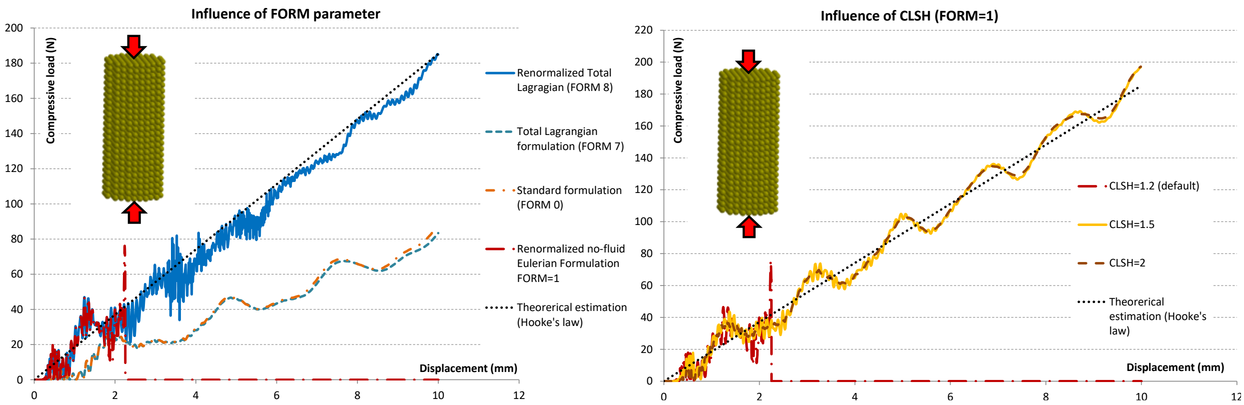

Fig. 11. Influence of FORM and CLSH parameter on compressive stiffness

4.3.4 Evaluation of bird's substitute model

As mentioned previously, a hydrodynamic material model combined with linear EOS is applied for the modeling of gelatine bird model. The majority of numerical works [9], [40], [12], [10], [7], [42] has been focused on the experimental pressure profile at the centre of impact, published by [16] , as means of verification. However, the pressure profile is highly affected by the resonant excitation of transducers providing high-frequency noise [16]; and therefore, the used experimental data can lead to erroneous setting of numerical model. According to the authors, the estimation of force-time history which is exerted by bird impact is of greater importance than the central pressure profile. The maximum force and the total transferred momentum (or impulse) obtained by integrating the force history provide better insight of loading condition. For this reason, the current study was based on the experimental study of [15], where the peak force and the impulse have been calculated for four different impact velocities of a 600 g bird. According to the authors' knowledge, this experimental data has been already used in [43] for the validation of a tabulated EOS. Therefore, the V.Walvekar's results will be taken into consideration for the evaluation of current study's model.

In the framework of present work, a more geometrically representative model using linear EOS is examined in relation to that of V.Walvekar [43]. In parallel, both the literature experimental results

[15] and the numerical results [43] are correlated with the simulation results derived from the current approach. In particular, experimental tests published in [15] were numerically replicated using the LS-DYNA software. A 600 g bird's substitute modelled by SPH particles was launched against the end of a 4.8m long, circular, aluminium bar with 127 mm diameter (Fig. 12~~Fig. 12~~); and four different analyses were carried out at impact velocity levels of 192 m/s, 219 m/s, 249 m/s and 269 m/s. The projectile is modelled as a hemispherical-ended cylinder with 9520 uniformly distributed particles with 4 mm PD (Fig. 12~~Fig. 12~~), whereas its assumed diameter (d=68mm), length (l=192 mm) and density (ρ=973 kg/m^3) are obtained by certain empirical formulas provided in [44]. Regarding the results, it should be mentioned that no filtering is applied to the numerical force-time responses presented below.

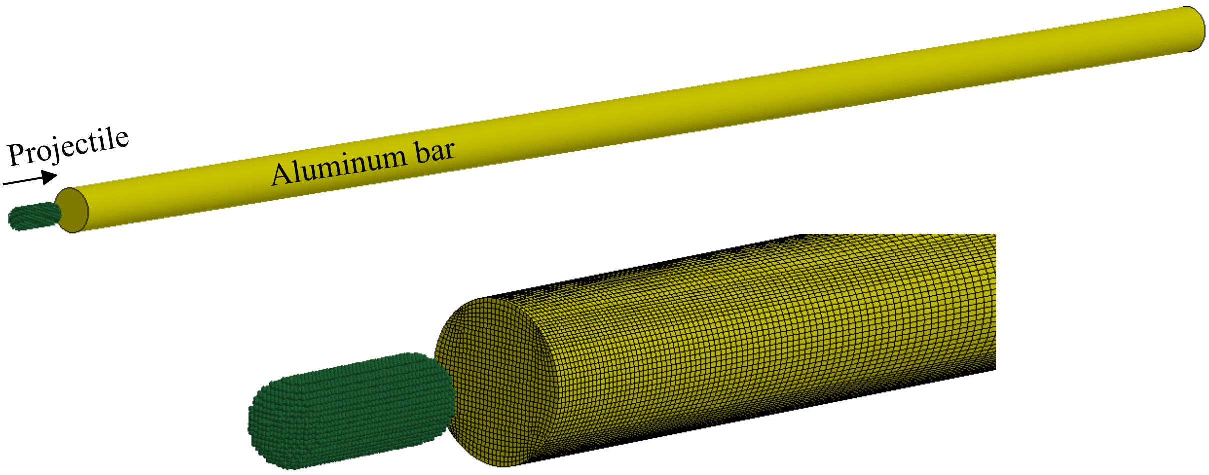

Fig. 12. Model of bird strike on aluminum target.

The Fig. 13~~Fig. 13~~ provides a comparison of the numerical force-time profiles for linear (section 4.2), polynomial and Gruneisen EOS in the case of 192 m/s (graph 'a'); it shows the numerical force histories for all impact velocities adopting the linear EOS and it cites the theoretical stagnation force and the theoretical impact duration in graph 'b'. Also, it correlates the non-dimensional peak force and non-dimensional impulse derived from current simulation study with the numerical and experimental ones taken from literature in graphs 'c' and 'd' of Fig. 13~~Fig. 13~~. The constants of polynomial and Gruneisen formulas was obtained from [11] and [9], [40], respectively. The non-dimensional peak force and impulse were calculated by the following generic equations for rigid target:

$$\textit{Non-dimensional Peak Force} = \frac{\textit{Numerical peak value}}{\textit{Theoretical stagnation value}} = \frac{F_p * l}{m * v^2 * \sin\theta} \qquad \text{Eq. 14}$$

$$\textit{Non-dimensional Impulse} = \frac{\textit{Numerical Impulse}}{\textit{Theoretical Impulse}} = \frac{\int F\,dt}{m * v * \sin\theta} \qquad \text{Eq. 15}$$

where F_p is the peak force obtained by graph ‘b’ of Fig. 13~~Fig. 13~~, m is the mass of bird, v is the impact velocity, l is the length of bird and θ is the impact angle. The theoretical impact duration and stagnation force were calculated by Eq.16 and Eq.17, respectively:

$$\textit{Theoretical impact duration} = \frac{l}{v} \qquad \text{Eq. 16}$$

$$\textit{Theoretical stagnation force} = \frac{m * v^2 * \sin\theta}{l} \qquad \text{Eq. 17}$$

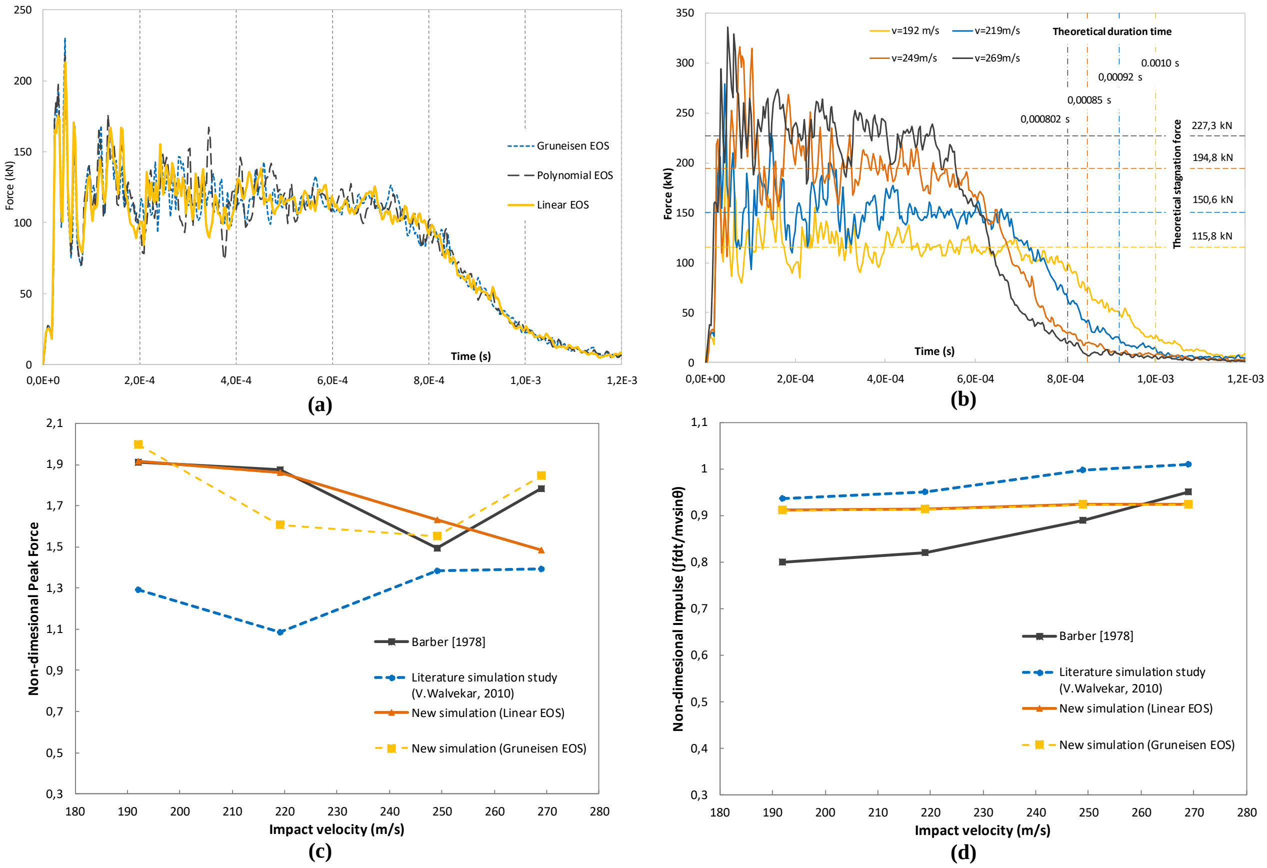

Fig. 13. Numerical force histories (a, b), Non-dimensional Peak Force (c) and Impulse (d).

Observing the Fig. 13~~Fig. 13~~, the following conclusions are inferred: a) the trend of numerically derived impact force history does not change by the type of EOS (graph ‘a’); b) the simulated and the experimental non-dimensional peak forces are identical in the cases of 192 m/s and 219 m/s when linear EOS is used, however the simulation significantly diverges from tests for impact velocities higher than 250 m/s (graph ‘c’); c) unlike, the Gruneisen EOS presents better results for impact velocities equal to 249 m/s and 269 m/s; d) the simulations executed in current study showed remarkably better results, in terms of non-dimensional peak force and impulse, in relation to V.Walvekar’s numerical work (graph ‘c’ and ‘d’); e) the influence of EOS formula on the non-dimensional impulse is negligible according the graph ‘d’ of Fig. 13~~Fig. 13~~; h) finally, the numerical stagnation force and impact duration using the linear EOS are in good agreement with theoretical ones for all impact velocities (graph ‘b’). In this section, it was proved that the hydrodynamic material model combined with zero dynamic viscosity, linear EOS and the proper SPH parameters presents excellent results in terms of peak force for impact velocities lower than 219 m/s; whereas the numerically predicted impulse is closer to experimental one, in any impact condition, in comparison with the V.Walvekar’s prediction.

4.4 Validation of the HF model results against the Experiments

In this section, the numerical results of HF model using the two different SPH configurations are presented. Initially, the numerical contact force histories are discussed; then, the numerical strain histories are compared with the results derived by test campaign; afterwards, the numerical and experimental evolution of projectile’s deformation are correlated; and finally, the interlaminar damage of CFRP faces is assessed.

4.4.1 Numerical force-time response

The Fig. 14~~Fig. 14~~ illustrates the numerical contact force histories obtained from the simulation with the HF model using the two different projectile’s models. Initially, it is observed that the model with 5 mm PD provides larger oscillations at contact force-time diagram in relation to 2 mm PD model, which is definitely linked with the contact gap formed by the particles distance. The peak force is found equal to 30.6 kN and 28.8 kN for 5 mm and 2 mm PD model, respectively. However, the impulse constitutes a more reliable indicator for model verification than the maximum force due to the aforementioned numerical oscillations. The difference between impulse values of two models is within 2.4%, which is acceptable range.

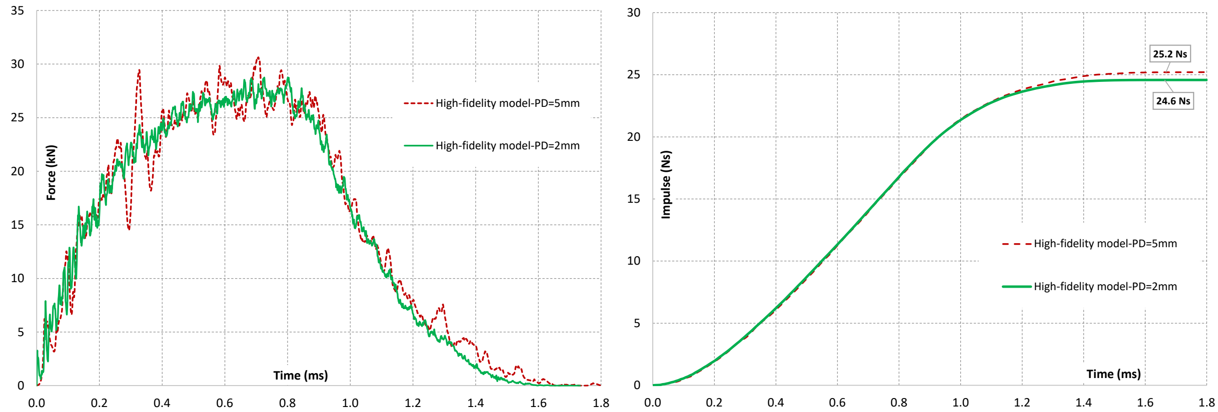

Fig. 14 Numerical contact force histories and impulse values (HF model)

4.4.2 Numerical and experimental strain histories

Fig. 15 depicts the experimentally measured strain histories obtained from four FBG sensors (P1_S1, P1_S3, P2_S1 and P2_S3) and the corresponding numerical results computed from HF model. The locations of measurements were clearly specified in Fig. 6~~Fig. 6~~. From numerical point of view, each numerical strain-time profile was calculated from the output strain data of corresponding solid element located on the back side of target structure.

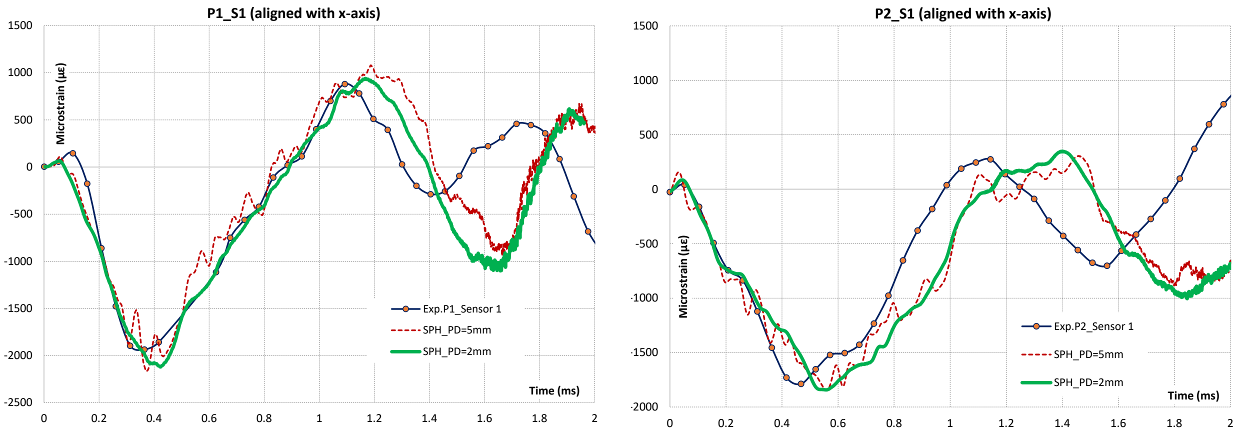

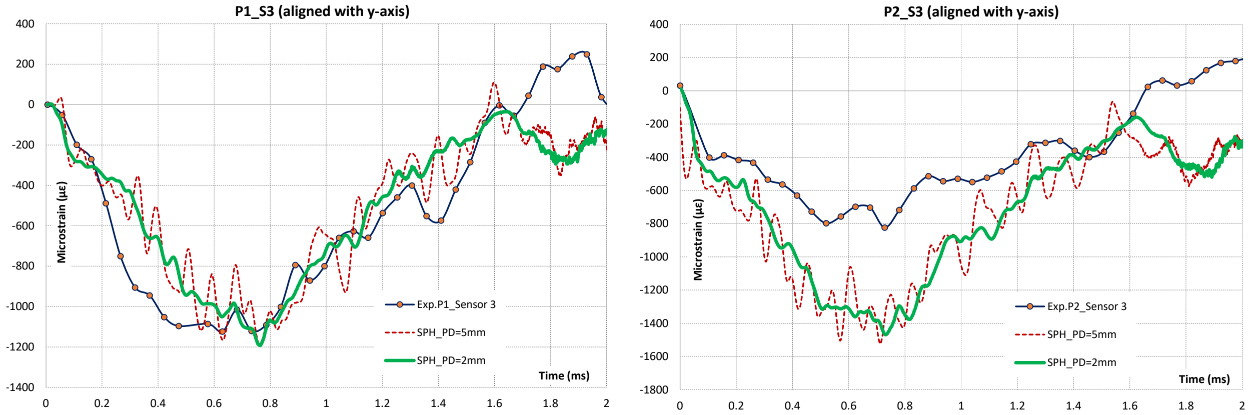

Fig. 15 Correlation of the HF numerical strain-time profiles with the experimental ones (based on global coordination system of Fig. 6~~Fig. 6~~).

It should be mentioned that the numerical strain data is an average obtained from the 8 integration points of solid element since fully integrated element formulation has been used for the composite skins modeling. The data recorded by sensors P1_S2 and P2_S2, which are located at the centre of the target back skin, were excluded here due to the signal loss emerged from the sensor-panel interface failure.

It is observed in Fig. 15 that high-frequency oscillations arose in the strain histories of 5 mm PD model due to the sparse distribution of SPH particles. However, both the strain amplitude and the period of strain histories of the coarse model (dashed red curves) are very close to the fine model (continuous green curve). Therefore, in terms of strain histories, the coarse SPH model of gelatine projectile (Fig. 8~~Fig. 8~~) can successfully substitute the finer model reducing the computational time from 18 hours to 14.5 hours (-19.4%).

The correlation of simulations with the impact tests was focused on the time interval from the impact initiation (t=0 ms) and the full projectile disintegration when the force drops to zero level (t=1.8 ms); whereas it should be mentioned that the vibration monitoring of panels after the impact completion is out of the purpose of current work. The assessment of model is based on the following five evaluation criteria: a) the initial slope of strain curve which describes the strain rate in elastic regime, b) the oscillation amplitude which shows the maximum strain during the impact event, c) the rise time at which the maximum strain occurs, d) the decay time which is the time of strain decline from maximum value to zero level and e) the trend of strain history up to 1.8 ms. Table 4 illustrates the results of evaluation study for the four examined locations.

Starting from the last sensor, P2_S3, it is observed that the numerical model can successfully capture the initial strain rate (t<0.05 ms), the rise time and the trend of experimental strain history. But significant divergence on strain amplitude is noted. The flattening of the strain signal at 0.12 ms might be due to FBG being partially detached. At that moment, any relaxation of strain is not expected since the impact has not been finished and no damage was observed. Therefore, the P2_S3 sensor's data is not valid to be used for the verification of HF model results. But the trend matching and the synchronization between the experimental and numerical strain history are powerful qualitative indicators that the actual panel response is similar with the numerical one. Unlike, the virtual strain sensor at location P1_S3 seems to predict excellently the maximum strain and rise time regardless the problem's complexity, since the corresponding calculated errors are 6.1% and 3.5%, respectively. Also, even though the interrogator's sampling frequency is marginal, the model's accuracy in the prediction of strain variation with time is very good.

	Evaluation criteria				
Location	**Accuracy on initial strain rate** (qualitative)	**Maximum strain** (με)	**Rise time** (ms)	**Decay time** (ms)	**Accuracy on history trend** (qualitative)
P1_S1	Medium	**Sim.:** -2120 **Exp.:** -1935 error: 9.5%	**Sim.:** 0.42 **Exp.:** 0.37 error: 13.5%	**Sim.:** 0.47 **Exp.:** 0.52 error: -9.6%	High
P2_S1	Extremely high	**Sim.:** -1840 **Exp.:** -1790 error: 2.7%	**Sim.:** 0.53 **Exp.:** 0.48 error: 10.4%	**Sim.:** 0.6 **Exp.:** 0.52 error: 15.3%	High
P1_S3	High	**Sim.:** -1190 **Exp.:** -1121 error: 6.1%	**Sim.:** 0.76 **Exp.:** 0.734 error: 3.5%	**Sim.:** 0.73 **Exp.:** 0.79 error: -7.5%	High
P2_S3	High	sensor debonding	**Sim.:** 0.73 **Exp.:** 0.72 error: 1.4%	**Sim.:** 0.96 **Exp.:** 0.86 error: 11.6%	High

Table 4. Evaluation criteria for the HF model validity

In the case of sensor P2_S1, it was observed that the model's performance is extremely high in terms of initial strain rate and the maximum strain. In particular, the virtual sensor has precisely recorded the strain variation from t=0 ms to t=0.32 ms; whereas, the first two strain spikes have been computed in a great extent. However, the numerical strain history presents a low hysteresis of 0.05 ms starting from t=0.32 ms, which increases to 0.26 ms for t>1.2 ms. By the examination of model was noted that this temporal lag is induced due to the instant softening of panel structure caused by the upper skin damage enlargement. Nevertheless, it is concluded the aforementioned panel's softening does not seem to be of high significance since the peak strain values have not been changed remarkably in relation to experimental ones. A significant difference between the experimental and numerical damage would lead to a dramatic change to the panel deformation and, therefore, to the strain field at the rear face. Finally, concerning the P1_S1 sensor, excellent matching between the experimental and numerical maximum strains (1st and 2nd peak values) is noted; the corresponding errors are 9.5% and 5.4%, respectively.

4.4.3 Evolution of soft body deformation

In this section, the experimental observed and the numerically obtained history of deformations of the soft body are correlated. The sequence of the frames captured by the high-speed camera, starting from the initial contact until the gelatine projectile disintegration, are shown in Fig. 16. The snapshots demonstrate clearly the hydrodynamic behavior of gelatine projectile during the impact, which is consistent with the published experimental results in [17], [18]. More importantly, quantitative correlation between the numerically obtained and experimentally observed projectile diameter in contact with the target is clearly demonstrated in Fig. 16. The maximum difference between the numerical and the actual values is 5.5% for t=0.5 ms, which is a very good agreement. Also, it can be concluded that the simulation results for the diameter raise rate agrees with the experiment and that the radial pressure distribution has been simulated properly. Finally, the final snapshot in Fig. 16 suggests that no significant fibre and matrix damage exists on the outer ply of front skin since no visible cracks have developed. The same conclusion is validated by the simulation results.

<table>
<tr><th>Time</th><th>HF model-2mm PD</th><th>Test</th><th>Comparison</th></tr>
<tr><td>0.50 ms</td><td>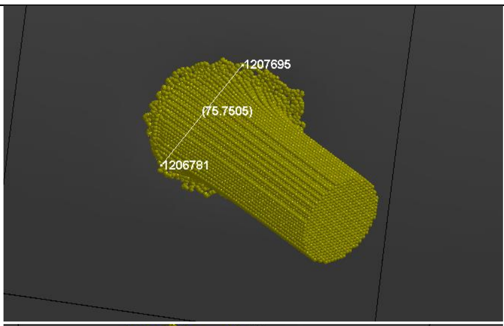</td><td>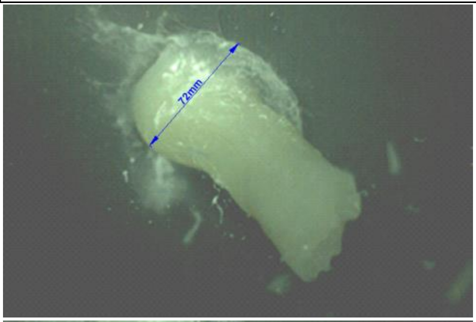</td><td>Num: 76 mm
Exp: 72 mm</td></tr>
<tr><td>0.70 ms</td><td>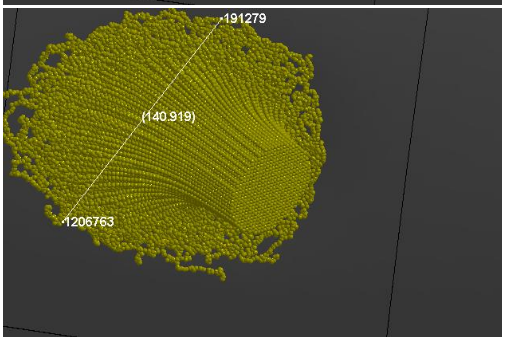</td><td>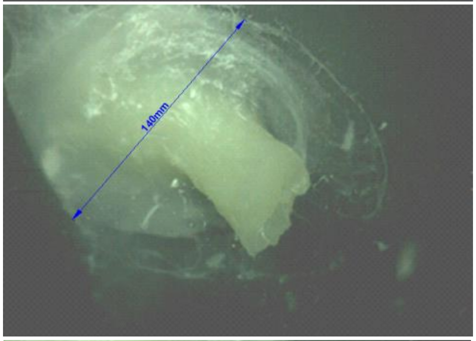</td><td>Num: 141 mm
Exp: 140 mm</td></tr>
<tr><td>0.90 ms</td><td>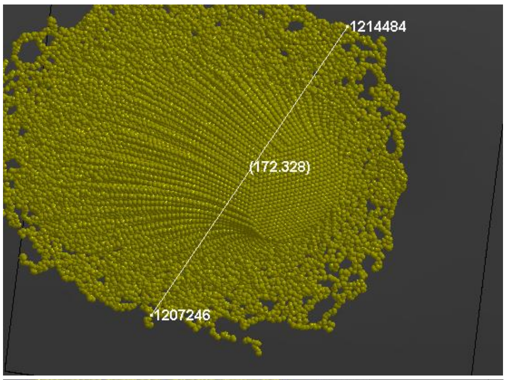</td><td>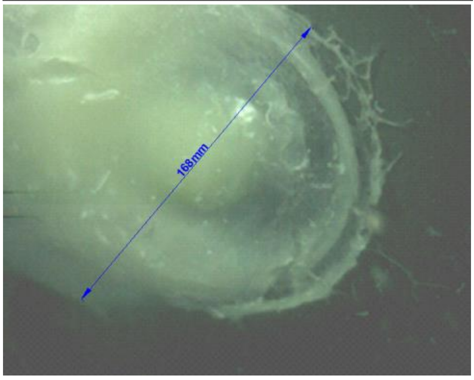</td><td>Num: 172 mm
Exp: 168 mm</td></tr>
<tr><td>1.10 ms</td><td>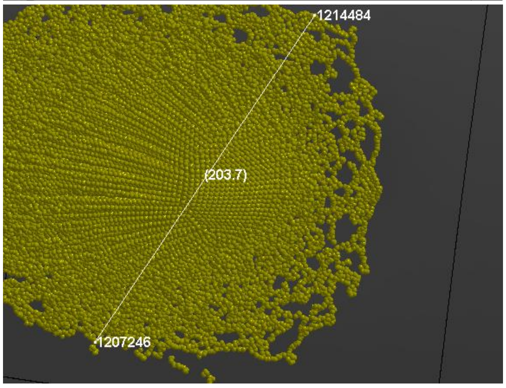</td><td>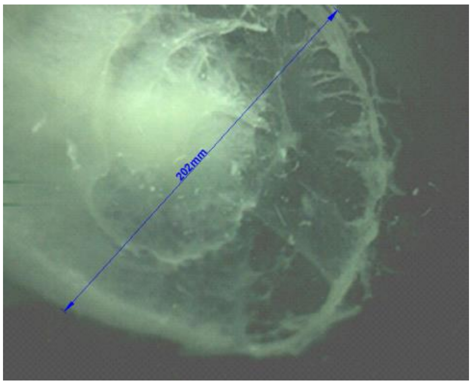</td><td>Num: 204 mm
Exp: 202 mm</td></tr>
<tr><td>1.80 ms</td><td>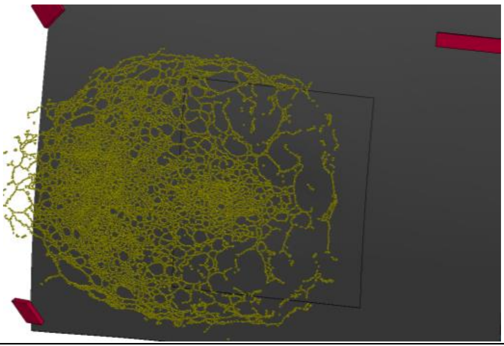</td><td>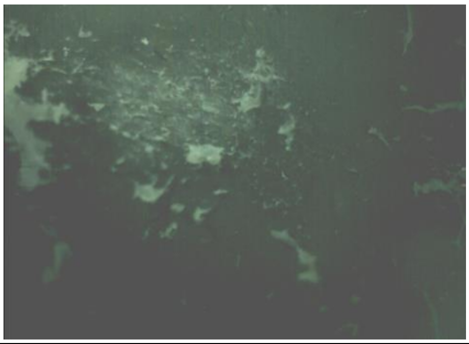</td><td>Num: - mm
Exp: - mm</td></tr>
</table>

Fig. 16 Snapshots of impact taken from the HF simulation and the experimental test.

4.4.4 Damage evaluation

To characterize the internal damage occurred after the impact test, Phased Array Ultrasonic Testing (PAUT) investigations were conducted by UBATH. PAUT methods employ a pulser-receiver piezo-electric elements array to steer an ultrasonic constructed wave trough the material and capture any anomalous refractions or phase shift of the wave propagating back, due to internal defects. A 5MHz 128 channels Phased-Array transducer was used to perform ultrasonic inspection of the impacted area. The scanned area of 198.5 mm x 160 mm is shown in Fig. 17a.

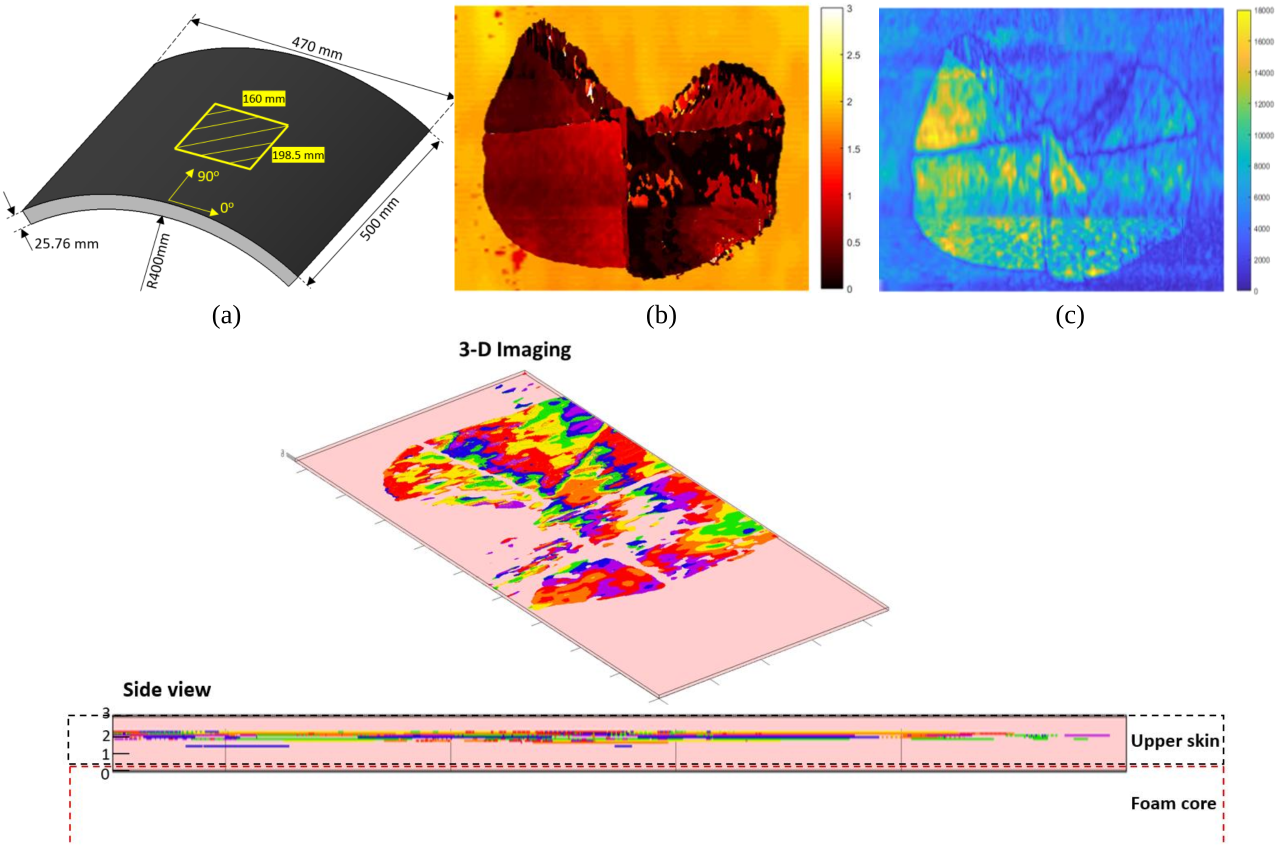

Fig. 17. Inspection results: (a) Scanned area, (b) Time of flight (TOF) C-scan damage imaging, (c) Amplitude C-scan, (d) 3-D damage imaging and side view.

The complex nature of an impact damage in sandwich panel is presented in the Time-of-flight (TOF) C-scan in Fig. 17b, where the color scale denotes the damage position inside the thickness; whereas, the amplitude of ultrasonic signal is shown in Fig. 17c. The amplitude peaks location can be related to the damage locations through the panel thickness. The total delaminated area by non-destructive evaluation is 16,875 mm^2, whereas the cumulative numerical damage is slightly larger and equal to

19,228 mm^2 (Fig. 18). This discrepancy might be due to the asymmetric delamination pattern observed in the experimental results. A heterogeneity of gelatine projectile and an imperfection in the target material might be possible reasons. However, the extent of experimental damage in both directions have been precisely captured by the HF model (Fig. 18).

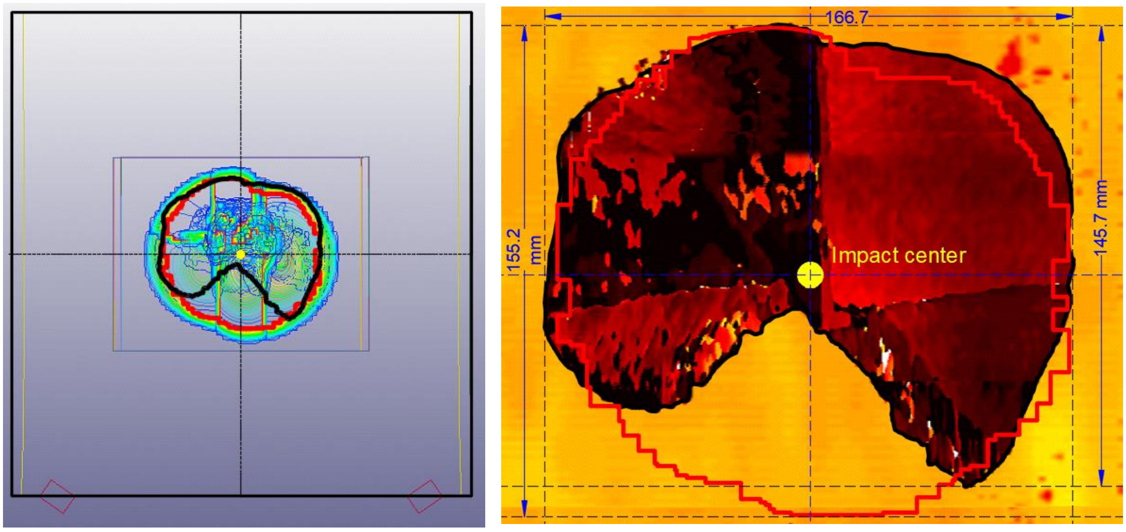

Fig. 18. Comparison of total numerical delamination damage (red line) with the experimental one (black line).

As shown in Fig. 17d and Fig. 19, impact cracks penetrate down to a depth of 1.439 mm (i.e. 1.561 mm from the reference bottom T=0 mm), and delamination only grew in the upper part of the skin, at a depth of 1.150 mm (i.e. 1.849 mm from the reference bottom T=0 mm). Therefore, it can be concluded that the impact damage has been confined at the upper skin of panel, and no interfacial damage between foam and upper skin exists (T=0.12mm).

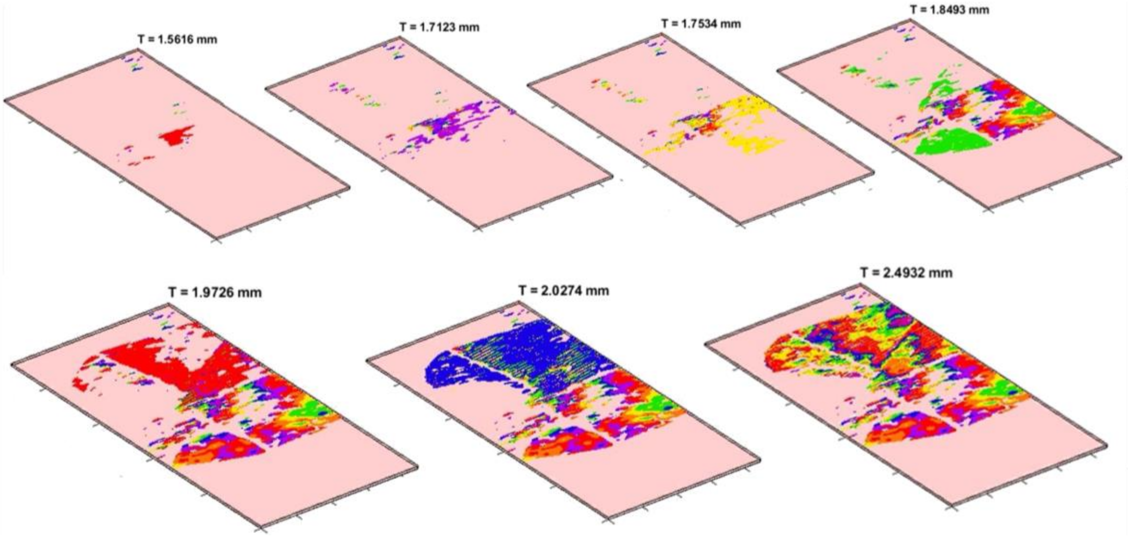

Fig. 19 Framed 3D-view of experimental damage at different thickness position T

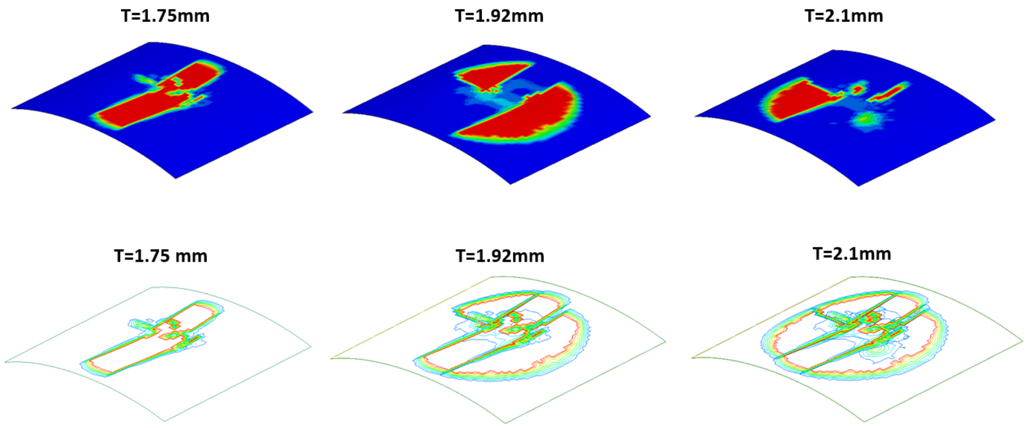

Fig. 20 Framed 3D-view of numerical interlaminar damage at upper skin: per interface for 3 sequential interfaces (top), cumulative damage (bottom).

The same conclusion can be also extracted by the numerical simulation, where the interface damage occurs only to three interfaces at the middle of upper skin. Fig. 20 illustrates the numerical interlaminar damage at the different positions.

5 Development of low-fidelity (LF) model

5.1.1 LF modeling approach

LF model targets to reduce the high computational time of HF one keeping the modeling accuracy to an acceptable level. It is well known that the most representative the model is, the most time-consuming it is. Therefore, for the sake of computational efficiency, the current approach is focused on the relegation of accuracy of damage modeling applying layered solid elements for skins. The 8-node layered solid elements in LS-DYNA use one integration point per layer for computational efficiency, and no limit exists to the number of integration points though the thickness [35]. The present study was based on the thick shell form 5 of LS-DYNA, where the through-thickness orientation of the integration points provides the ability to the element to model the stacking sequence and to capture the bending stiffness and the through the thickness stresses like a 3D solid element [29]. The validity of this element type was verified to 3-point bending loading in Table 3~~Table 3~~. From the material model point of view, the same constitutive and failure law (MAT_54) were applied as previously. The second modification in relation to the HF simulation approach is that no cohesive elements are implemented into the CFRP faces for the capturing of interlaminar damage. Thus, the running time was significantly reduced. Regarding the foam material model and the interface between that and faces, no modification is done. The LF model of sandwich panel with high-density SPH model of gelatine projectile is shown in Fig. 21. All simulations were executed using an Intel Xeon 3.5 GHz processor and a 16 GB RAM, and the running time is given in Table 5.

In parallel, a model with impulse-equivalent loading was built for the further mitigation of computational time (Fig. 21) and the estimation of its divergence from the LF/SPH model since it will constitute the LF numerical tool of digital-twin methodology. Essentially, it was based on the LF modelling approach for the case of sandwich panel, and it uses a time-variable, distributed, and impulse-equivalent load for the representation of bird impact force. The equivalent load is applied on a rectangular area, whose the edge length is equal to projectile’s diameter (50 mm), and which represents the main contact area during the impact. It is observed that the shape of loading for 45^{o} oblique soft-body impact, shown in Fig. 22~~Fig. 22~~, looks like a symmetrical bell; therefore, it can be simplified as a tri-linear loading curve. The equivalent loading curve is created keeping the values of impulse and maximum force equal to those of HF model and adopting similar loading and unloading rates. The applied equivalent load is presented in ‘a’ graph of Fig. 22~~Fig. 22~~, whilst the computational time of three different models is presented in Table 5. Using LF/equivalent model, a 68% decrease of running time was achieved in comparison to the LF/SPH model.

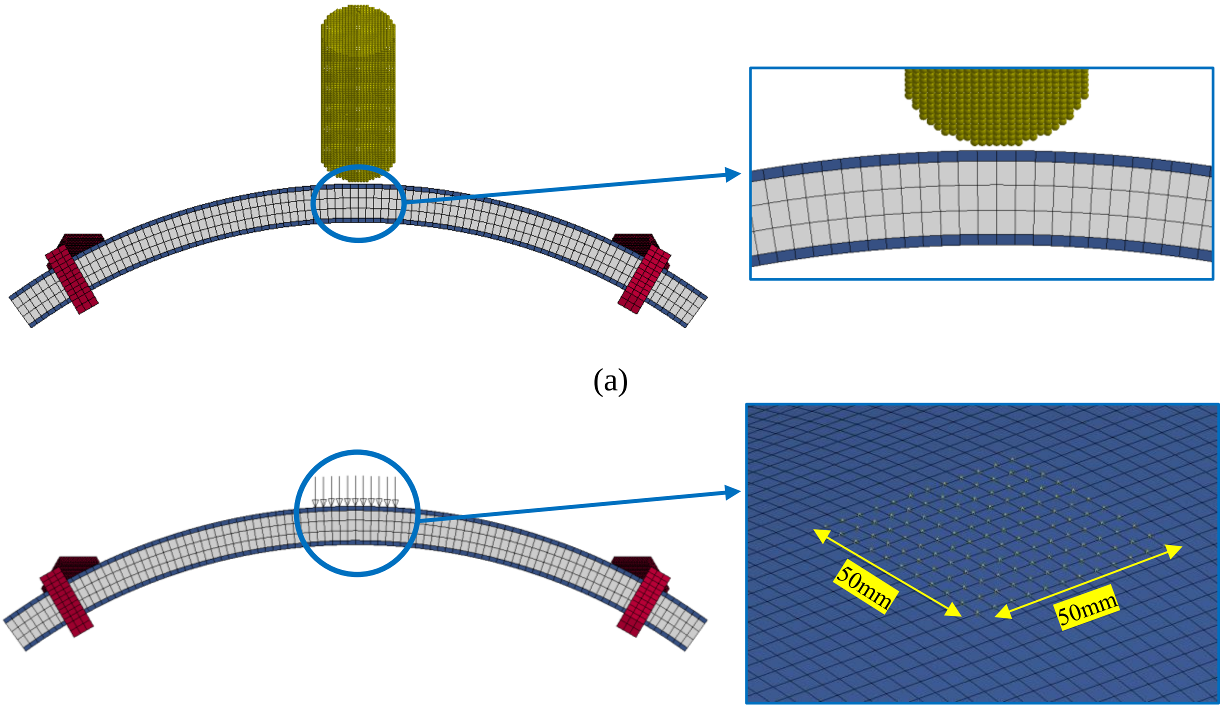

(a)

(b)

Fig. 21 LF model using a) SPH projectile (LF/SPH) and b) impulse-equivalent loading (LF/equivalent)

Model	**Computational time**
HF/SPH model (2 mm PD)	18.0 hr
HF/SPH model (5 mm PD)	14.5 hr
LF/SPH model (2 mm PD)	19 min
LF/equivalent	6 min

Table 5. Running time of models (up to the instant of 2.0 ms)

5.1.2 Models comparison

Looking the results of HF/SPH and LF/SPH models in Fig. 22~~Fig. 22~~, it is noted that the impulse of latter one diverges only by 2.0% from that of former. Essentially, it slightly underestimates the impulse of HF model. Regarding the force-time history, it is inferred that the difference is almost negligible since the peak force error between the two analyses is equal to 0.36%; whereas, the impact durations are identical.

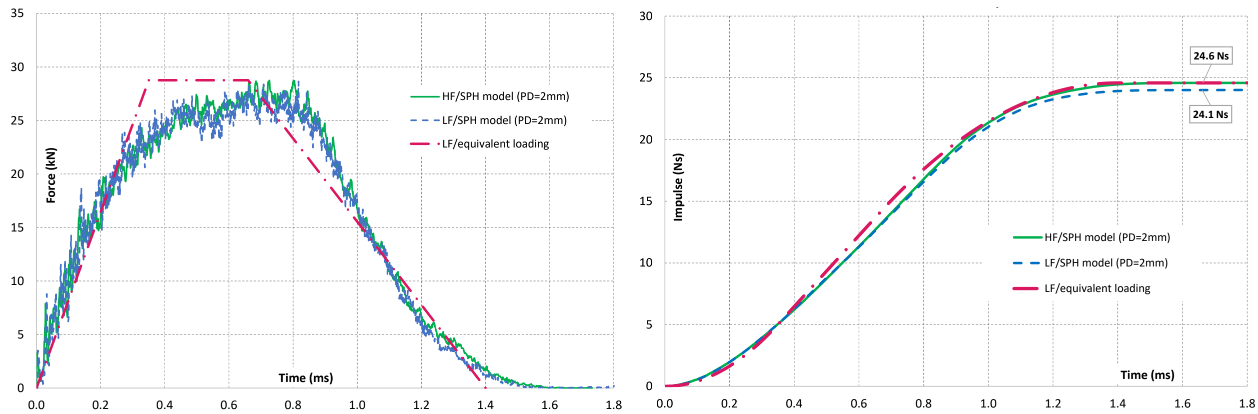

Fig. 22 HF/SPH vs. LF/SPH vs. LF/equivalent contact force histories and impulse values

As far as the strain histories are concerned, it was observed that both LF/SPH model and LF model with impulse-equivalent loading are in good agreement with the trend of strain history derived from HF model (Fig. 23~~Fig. 23~~). The LF models might be limited in predicting the actual strain rate of loading and unloading as well as the actual peak strain values due to their inability to simulate accurately the skins' damage. However, in Fig. 23~~Fig. 23~~, the rise and decay times are relatively close to those of HF model, which are quantitative indicators that the global vibrational response of panel structure can be estimated. The LF model is headed in the right direction, therefore it can be used as a quick tool for the identification of the impact loading correlating the numerical strain histories with experimental ones. The LF model should be capable of estimating the required loading data, such as loading magnitude, the impact duration, the total impulse, the impact angle, and the position of impact, which is obviously unknown during the digital-twin assisted damage diagnosis.

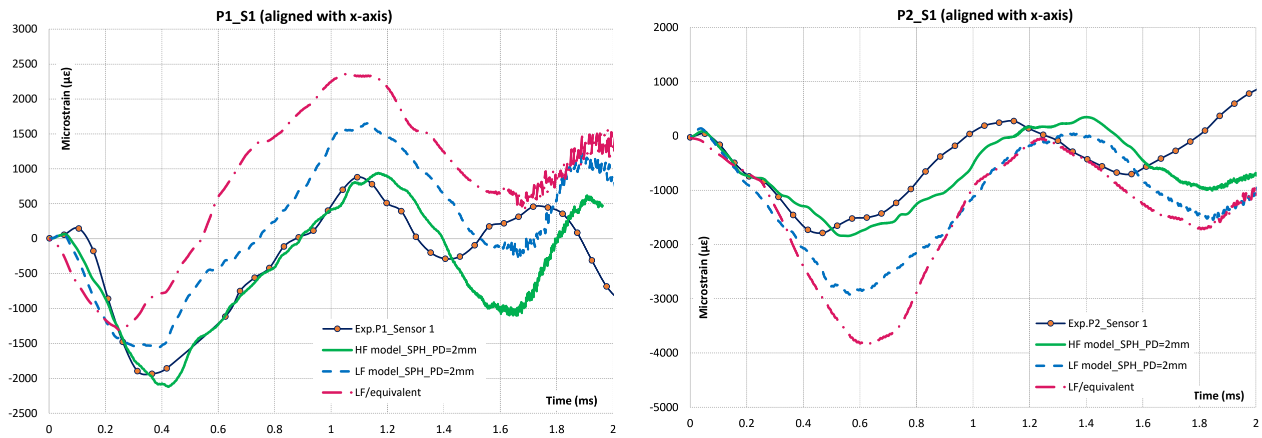

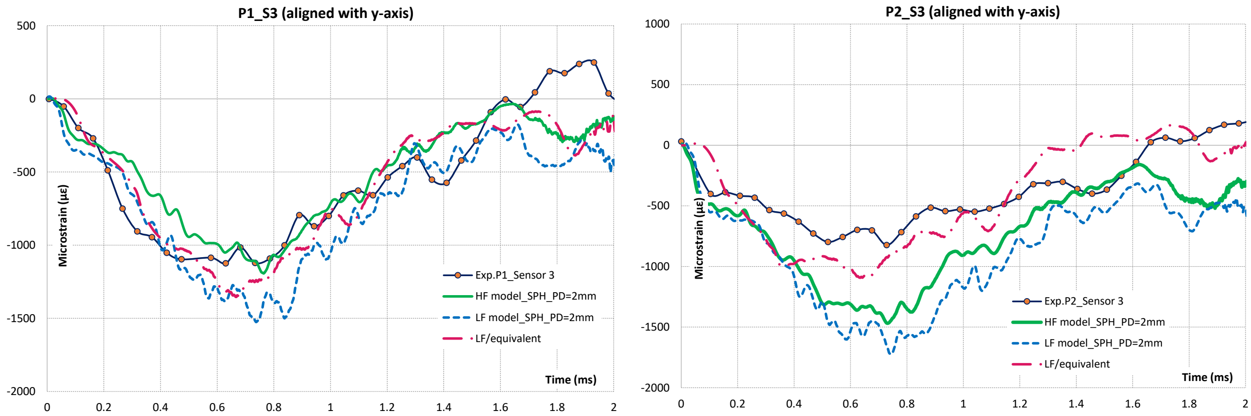

Fig. 23~~23~~ HF/SPH vs. LF/SPH vs. LF/equivalent numerical strain-time profiles

The Fig. 24 compares the fringes of resultant displacements of the HF/SPH model with those of the LF/equivalent model at three different time instants. The contour lines display graphically the boundaries of displacement change. In general, similarity between the two models can be observed in terms of the displacement magnitude, the rate of deformation and the deformed area. Small differences on the extension of the deformed area and the maximum displacement can reasonably exist, and they are acceptable due to the difference on the method of load application. In the case of HF model, the load is both temporally and spatially variable using a moving SPH projectile, whereas, in the case of LF with impulse-equivalent loading, it is only temporally variable. In conclusion, it can be inferred that the LF model can sufficiently approximate the HF model deformation.

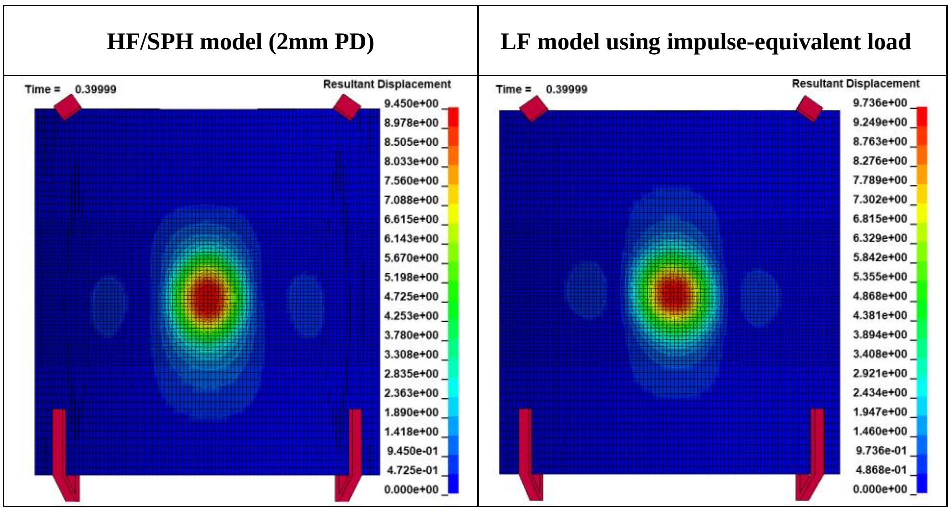

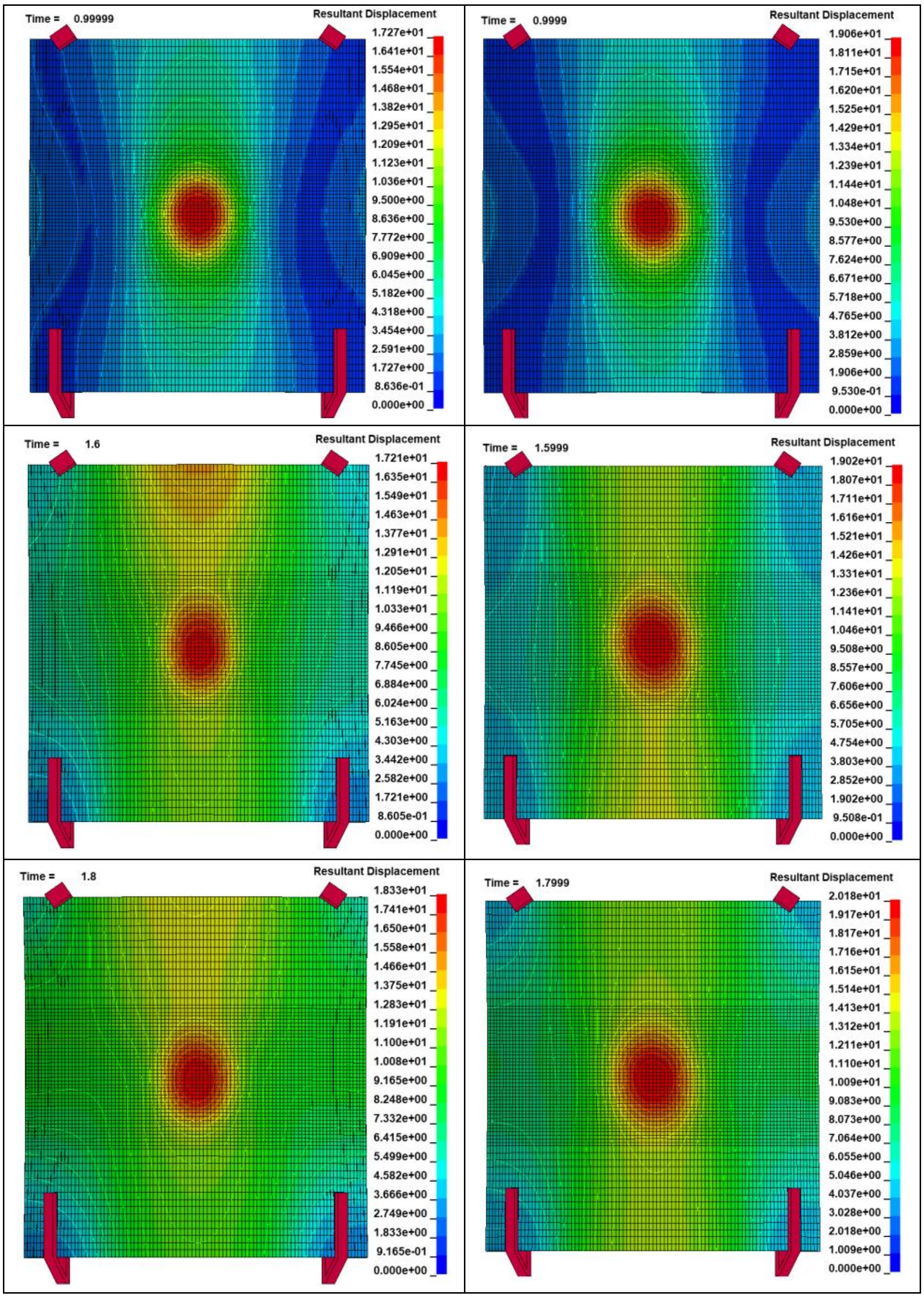

Fig. 24 Fringe of resultant displacements of HF/SPH model and LF/equivalent model (mm)

6 Conclusions

The dynamic response of a curved composite sandwich panel subjected to soft body impact was investigated both numerically and experimentally. In particular, two computational tools with different simulation fidelity and computational cost were developed. Firstly, a high-fidelity FE/SPH model was established, and it was validated using the soft body impact experimental results. Afterwards, a time-efficient low-fidelity model was created and was correlated with the former. It was concluded that the high-fidelity model can sufficiently approximate the experimental strain histories recorded by the FBG sensors, with the experimental delamination area accurately predicted. On the other hand, the LF model can rapidly predict the global vibrational response of sandwich panel; further transformation of the LF model based on applying an impulse-equivalent loading instead of SPH model of the soft projectile, reduced the total computational time by 68%.

In conclusion, the LF model can be used as a quick numerical guide for the identification of impact loading conditions comparing the numerical results with the real-time strain histories taken from FBG sensors. Knowing the loading condition, HF model can employ as virtual detector and estimator of sandwich panel damage avoiding the traditional fault diagnosis techniques. The development of digital-twin-assisted damage diagnosis method using the current numerical tools will be presented in a future paper. Finally, the assessment of influence of strain rate and the impact conditions (i.e., impact velocity and angle) constitutes future work.

Acknowledgements

This work has been supported by EU, H2020 Smart, Green and Integrated Transport, Aviation program under the acronym EXTREME (Project reference 636549). The authors would like to specially thank Technobis TFT-FOS for its support on the processing of experimental data.

Bibliography

[1] Accident Report. Accident occurred to the Boeing B737-800AS aircraft, Italian Agengy for Fight Safety, Rome, November 2018

[2] Accident Report. Loss of Thrust in both engines after enountering a flock of birds and subsequent ditching on Hudson river US Airways Flight 1549, National Transportation Safety Board, Washingthon, May 2010

[3] Hereson H. EASA views on Rotorcraft bird strike threat. European Aviation Safety Agency, 2016.

[4] Certification Specifications and Acceptance Means of Compliance for Large Rotorcraft CS-29-Amendment 4, European Aviation Safety Agency, November 2016.

[5] Lavoie MA, Gakwaya A, Ensan M, Zimcik D. Review of existing numerical methods and validation procedure available for bird strike modeling. Int. Conf. Comp. Exper. Eng. Sci., 2007; 2:4. doi:10.3970/icces.2007.002.111

[6] Smojver I, Ivancevic D. Bird strike damage analysis in aircraft structures using Abaqus/Explicit and coupled Eulerian Lagrangian approach. Comp. Sci. Technol.,2011;71:4. https://doi.org/10.1016/j.compscitech.2010.12.024

[7] Jang JH, Ahn SH. Bird-strike damage analysis and preliminary design of composite radome structure using smoothed particle hydrodynamics. Appl. Compos. Mater., 2019; 26. doi.org/10.1007/s10443-018-9750-9.

[8] Guida M, Marulo F, Meo M, Russo S. Certification by birdstrike analysis on C27J fullscale ribless composite leading edge. Int. J. Impact Eng., 2013; 54. https://doi.org/10.1016/j.ijimpeng.2012.10.002

[9] Hedayati R, Ziaei-Rad S. A new bird model and the effect of bird geometry in impacts from various orientations. Aerosp. Sci. Technol., 2013; 28:1. https://doi.org/10.1016/j.ast.2012.09.002

[10] Hedayati R, Ziaei-Rad S. Effect of bird geometry and orientation on bird-target impact analysis using SPH method. Int. J. Crashworthiness,2012; 17:4. https://doi.org/10.1080/13588265.2012.674333

[11] Vignjevic R, Campbell J, Hughes K, et al. Soft body impact resistance of composite foam core sandwich panels with unidirectional corrugated and tubular reinforcements. Int. J. Impact. Eng., 2019;132. https://doi.org/10.1016/j.ijimpeng.2019.103320

[12] Heimbs S, Bergmann T. High-velocity impact behavior of prestressed composite plates under bird strike loading. Int. J. Aerospace Eng., 2012; 372167. doi:10.1155/2012/372167, 2012.

[13] Eren Z, Taratoglu S, Balkan D, Mecitoglu Z. Modeling of bird strike on a composite helicopter rotor brade. J. AIAA, 2017. https://doi.org/10.2514/6.2017-1991, 2017.

[14] Qiu J, Wang D, Chuanjun L, Chen L, Huang H, Sun Q. Dynamic response of bird strike on honeycomb-based sandwich panels of composite leading edge. Int. J. Crashworthiness, 2020. https://doi.org/10.1080/13588265.2020.1718466.

[15] Barber J, Taylor H, Wilbeck J. Bird Impact Forces and Pressures on Rigid and Compliant Targets. Technical Report AFFDL-TR-77-60, University of Dayton, Ohio, 1978.

[16] Wilbeck J. Impact behavior of low strength projectiles. Technical Report AFML-TR-77-134. Wright-Patterson Air Force Base, Ohio, 1978.

[17] Lavoie MA, Gakwaya A, Ensan M, Zimcik DG, Nandlall D. Bird's substitute tests results and evaluation of available numerical methods. Int. J. Impact Eng., 2009; 36:10-11. https://doi.org/10.1016/j.ijimpeng.2009.03.009

[18] Pernas-Sanchez J, Artero-Guerrero J, Varas D, Lopez-Puente J. Artificial bird strike on Hopkinson tube device: experimental and numerical analysis. Int. J. Impact Eng., 2020; 138. https://doi.org/10.1016/j.ijimpeng.2019.103477

[19] Tuegel E.J, Ingraffea A, Eason T, Spottswood S.M. Reengineering aircraft structural life prediction using a digital twin. Int. J. Aerospace Eng., 2011; 154798. https://doi.org/10.1155/2011/154798

[20] Glaessgen E, Stargel D. The digital twin paradigm for future NASA and U.S. Air Force Vehicles. 53rd AIAA/ASME/ASCE/AHS/ASC Conf., Honolulu, Hawaii, April 2012. https://doi.org/10.2514/6.2012-1818

[21] Qi Q, Tao F, Hu T, Anwer N, Liu A, Wei Y, Wang L, Nee A. Enabling technologies and tools for digital twin. J. Manuf. Syst., 2019. https://doi.org/10.1016/j.jmsy.2019.10.001

[22] Drawing Database. Agusta Westland AW 139, http://drawingdatabase.com

[23] Technical data sheet CYCOM 977-2 epoxy resin system. Rev:01, Cytec Engineering Materials, 2012.

[24] Giannaros E, Kotzakolios A, Sotiriadis G, Kostopoulos V. A multi-stage material model calibration procedure for enhancing numerical solution fidelity in the case of impact loading of composites. J. Compos. Mater., 2020; 55:1. https://doi.org/10.1177/0021998320944992

[25] Elan-tech AS 89.1/ AW 89.2 material data sheet, ELANTAS Italia S.r.l.

[26] Giannaros E, Kotzakolios A, Kostopoulos V, Campoli G. Hypervelocity impact response of CFRP laminates using smoothed particle hydrodynamics method: Implementation and Validation. Int. J. Impact Eng. , 2019; 123. https://doi.org/10.1016/j.ijimpeng.2018.09.016

[27] Moura M.F.S.F, Campilho R.D.S.G, Goncalves J.P.M. Pure mode II fracture characterization of composite bonded joints. Int. J. Solids Struct., 2009; 46:6. https://doi.org/10.1016/j.ijsolstr.2008.12.001

[28] Tsokanas P, Loutas T, Kotsinis G, Brink W.M., Nijhuis P. Strain energy release rate and mode partitioning of moment-loaded elastically coupled laminated beams with hygrothermal stresses. Compos. Struct., 2020; 113237. https://doi.org/10.1016/j.compstruct.2020.113237, 2020.

[29] Hallquist J. LS-DYNA theory manual, 2006. Livermore Software Tehnology Corporation.

[30] Tabiei A, Zhang W. A zero thickness cohesive element approach for dynamic crack propagration using LS-DYNA. 15th Int. LS-DYNA Users Conf. , Dearborn, Michigan, 2018.

[31] Knight N. Factors influencing progressive failure analysis predictions for laminated composite structure. J. AIAA, 2008; 092407. https://doi.org/10.2514/6.2008-2108

[32] Gu J, Chen P. Some modifications of Hashin's failure criteria for unidirectional composite materials. Compos. Struct., 2017; 182. https://doi.org/10.1016/j.compstruct.2017.09.011.

[33] AIREX C70 material Data sheet EN 2010 V02, 2010.

[34] Wang R, Proust G, L. Shen. Characterizations of mechanical properties of two polymer foams under quasi-static and impact loading, University of Sydney, School of Civil Engineering, 2017. https://poster.quantumfi.net/images/posters/2017/pdf/characterizations-of-mechanical-properties-of-two-polymer-foams-under-quasi-static-and-impact-loading.pdf

[35] Hallquist J. LS-DYNA keyword user's manual R8.0. Livermore Software Tehnology Corporation.

[36] Fatehi R, Manzari M.T. Error estimation in smoothed particle hydrodynamics and a new scheme for second derivatives. J. Comput. Math. Appl., 2011; 61:2. https://doi.org/10.1016/j.camwa.2010.11.028

[37] Lacome J. SPH formulations: New developments in LS-DYNA. 7th European LS-DYNA users conference, Salzburg, 2009.

[38] Abrate S. Soft impacts on aerospace structures. Prog. Aerosp. Sci. 2016;81. https://doi.org/10.1016/j.paerosci.2015.11.005

[39] Challita A. Validation of a bird substitute for the development and qualification of aircraft transpareciles. Technical Report AFWAL-TR-80-3098. University of Dayton, Ohio, 1980.

[40] Hedayati R, Ziaei-Rad S, Eyvazian A, Hamouda A. Bird strike analysis on a typical helicopter windshield with different lay-ups. J. Mech. Sci. Technol., 2014; 28. https://doi.org/10.1007/s12206-014-0125-3

[41] Zenkert Dan. An introduction to sandwich structures. Student Edition, Stockholm, December 2005.

[42] Johnson A, Holzapfel M. Modeling soft body impact on composite structures. Compos. Struct., 2003; 61:1-2. https://doi.org/10.1016/S0263-8223(03)00033-3

[43] Walvekar V, Chandrashekhar T, Bhonge P, Lankarani H. Birdstrike analysis on leading edge of an aircraft wing using a smooth particle hydrodynamics bird model. ASME Int. Mech. Eng. Congr., 2012; IMECE2010-37667. https://doi.org/10.1115/IMECE2010-37667

[44] The hazared posed to aircraft by brids. Australian Transport Safety Bureau (ATSB), 2002. ISBN 1 877071 23 4